

UC Berkeley

UC Berkeley Electronic Theses and Dissertations

Title

Nonlinear Optical Properties of the Chiral Weyl Semimetal RhSi

Permalink

<https://escholarship.org/uc/item/3h5826gf>

Author

Rees, Dylan Nathaniel

Publication Date

2021

Peer reviewed|Thesis/dissertation

Nonlinear Optical Properties of the Chiral Weyl Semimetal RhSi

by

Dylan Rees

A dissertation submitted in partial satisfaction of the

requirements for the degree of

Doctor of Philosophy

in

Physics

in the

Graduate Division

of the

University of California, Berkeley

Committee in charge:

Professor Joseph Orenstein, Chair

Professor Feng Wang

Professor Jeffrey Bokor

Fall 2021

Nonlinear Optical Properties of the Chiral Weyl Semimetal RhSi

Copyright 2021
by
Dylan Rees

Abstract

Nonlinear Optical Properties of the Chiral Weyl Semimetal RhSi

by

Dylan Rees

Doctor of Philosophy in Physics

University of California, Berkeley

Professor Joseph Orenstein, Chair

Nonlinear optical properties of materials offer a diverse and powerful experimental probe into symmetry, electronic properties, and band structure. When paired with variable-wavelength light sources, these techniques are enhanced with the capability of resolving energy-dependent features. These properties are restricted to space groups that break inversion symmetry, but this dependence on crystal structure provides an opportunity to gain information about the material, and can help distinguish various electronic effects within a crystal. This point is crucial to this work, where bulk and surface optical properties in the Weyl semimetal RhSi are completely disentangled through symmetry considerations alone, with no need to rely on conjectures or assumptions about spectral features.

Weyl semimetals are a class of materials of special interest in condensed matter physics community within the last 10 years because their electronic band structures contain features which are analogous to Weyl fermions, a class of chiral fundamental particles which have not been observed in nature. While studied extensively experimentally, certain properties of Weyl semimetals have eluded measurement and theories have gone unconfirmed. One issue is that most Weyl semimetals only resemble an ideal model over a small energy range, limiting the optical sources available to study them within a relevant photon energy. Weyl semimetals may also contain trivial bands away from the Weyl fermion structures whose properties can be difficult to disentangle from those of interest.

In this work, nonlinear optical properties of the Weyl semimetal RhSi are measured. In particular, the theory of the Quantized Circular Photogalvanic Effect [35] in Weyl semimetals, a bulk property, is tested via measurements of terahertz generation and radiation. Precise numerical agreement with the theory is ruled out for the material, although we find the qualitative features of the prediction to hold true. Similar measurements are made in order to examine surface states on RhSi which have proven difficult to experimentally study with traditional transport and optical techniques. The bulk and surface properties are distinguished by considering experimental geometry in concert with crystal symmetry and orientation.

To my family.

Contents

Contents	ii
List of Figures	iii
List of Tables	vii
1 Berry Curvature and Weyl Semimetals	1
1.1 Berry curvature	1
1.2 Weyl Semimetals	4
2 Nonlinear Optics	9
2.1 Basic description	9
2.2 Frequency considerations in nonlinear optics	10
3 Bulk Photogalvanic Effects in RhSi	13
3.1 Photogalvanic effects and Weyl Semimetals	13
3.2 Experimental setup	16
3.3 PGE Symmetry	17
3.4 CPGE Spectrum	21
3.5 Calibrating the CPGE Spectrum	24
4 Surface Photogalvanic Effects	36
4.1 Surface States	36
4.2 Symmetry Considerations	38
4.3 Experimental Results	39
Bibliography	50

List of Figures

1.1	Berry phase paths Two paths in \mathbf{k} -space which will yield different Berry phases. Open paths (left) result in gauge-dependent Berry phases. Closed paths (right) result in gauge- <i>in</i> dependent Berry phases.	2
1.2	Basic Weyl semimetal model A basic model of a Weyl semimetal. There are two nodes with opposite signs as in Eq. 1.19. Integration of the Berry flux through the surface \mathcal{S} will yield the Chern number of the first Weyl node, as in Eq. 1.23.	4
1.3	Berry curvature in the Brillouin zone The total Chern number of all Weyl nodes in the Brillouin zone must be zero. This can be seen by the fact that the total Berry flux through the Brillouin zone boundary must be zero.	5
1.4	Weyl node symmetries Under inversion symmetry, the existence of a Weyl node at \mathbf{k} implies the existence of a Weyl node at $-\mathbf{k}$ with opposite Chern number. Under time-reversal symmetry, the existence of a Weyl node at \mathbf{k} implies the existence of a Weyl node at $-\mathbf{k}$ with the same Chern number.	6
1.5	Fermi arcs in Weyl semimetals Weyl semimetals have surface states which connect the projections of the bulk Weyl points onto the surface Brillouin zone. This can be seen by considering the Berry flux through slices of the Brillouin zone between the nodes.	7
2.1	Second order susceptibility spectrum Schematic of fundamental and second order susceptibility within a material. Light with frequency centered around ω produces electric fields in the material at dc and 2ω . These two effects are referred to as the photogalvanic effect and second harmonic generation, respectively. . .	11
2.2	Second order effects Schematic of fundamental light striking a material and producing second order effects. SHG light is radiated from the material with twice the frequency and a photogalvanic current (black arrow) is produced. For fundamental light with some frequency spread $\Delta\omega$, the photogalvanic current will have a small frequency and thus radiate.	12
3.1	Photocurrents from a Weyl node Schematic illustrating selection rules for optical transitions on a Weyl node with circularly polarized photons. With photon spin $s = +1$ (-1), only transitions on the right (left) side of the node will be allowed, leading to an asymmetric excited state and thus a photocurrent. . . .	14

- 3.2 **Weyl nodes and mirror symmetry** When mirror symmetry is present, nodes of opposite chirality are degenerate, and thus produce equal and opposing CPGE contributions. In a chiral system, nodes can be degenerate and thus optical transitions near one node can be Pauli blocked, leaving the CPGE from the other node unopposed. 15
- 3.3 **Experimental apparatus** (a) Schematic of experiment showing optical paths and optical elements. PD, photodiode; BS, beam splitter; $\lambda/2$, half-wave plate; $\lambda/4$ quarter-wave plate; WP, Wollaston prism. (b) Schematic showing flow of optical paths (red lines) and electronic references (dashed black lines) and signals (black lines) resulting in the measured value for the terahertz electric field. (c) 800nm optical pulses arrive at the photodiode at 5kHz, while the terahertz pulses arrive at 2.5kHz due to the optical chopper blocking every other pulse in the pump arm of the experiment. This allows for direct comparison of the electro-optical effect in ZnTe with the terahertz signal present and not present. A particular time delay Δt is chosen before taking a single measurement which is done by averaging a certain number of pulses, typically in the range 5000 – 25000 depending on the signal strength and noise level. 16
- 3.4 **Terahertz pulses** An example of terahertz pulses measured from RhSi using circularly polarized light at $\lambda = 2000\text{nm}$ 17
- 3.5 **Photocurrent symmetry** (a) Measurement of the THz polarization. Orange and green curves show the vertical and horizontal components of the pulse as a function of time. The reconstructed THz pulse (red curve) is then projected onto a plane, showing the direction of linear polarization, θ . (b) Dependence of the angle of LPGE terahertz polarization, θ , on angle of rotation of (111) face about the surface normal, ϕ , with pump at normal incidence. The relation $\theta = 3\phi$ predicted by the space group $P2_13$ symmetry is confirmed. The CPGE signal is below measurement noise level in this geometry. (c) Same as (b) except for 45° incidence. LPGE polarization again varies as $\theta = 3\phi$. CPGE is horizontally polarized independent of the crystal orientation confirming that the CPGE current is parallel to the pump wavevector. (d) Schematic showing that the resulting in plane CPGE current is fixed by the plane of incidence of the pump light. The CPGE current at normal incidence is normal to the surface of the sample and thus does not radiate into free space. 19
- 3.6 **CPGE spectrum** (a) CPGE amplitude $\beta\tau$ in units of $\frac{\pi e^3}{3h^2} \times \text{fs}$ as a function of photon energy, showing abrupt quenching above 0.65 eV. (b) Schematic showing the surface \mathcal{S}_ω in k -space defined by the available optical transitions at photon energy $\hbar\omega$. For $\hbar\omega < E_C$, \mathcal{S}_ω encloses a single node and has integrated Berry flux $C = \pm 4$. Above E_C it encloses two topological nodes of opposite chirality and $C = 0$. The blue shaded region in (a) indicates the region where \mathcal{S}_ω encloses only a single node. 21

3.7	Reflectivity and optical conductivity (a) Measured reflectivity of RhSi. (b) Optical conductivity determined by reflectivity measurements and Kramers-Kronig analysis (blue curve). The Drude peak is used to infer that the scattering time has value $\tau = 8.6$ fs. The orange curve represents the optical conductivity from the Γ and R nodes alone [56].	22
3.8	Crystal growth and diffraction Laue diffraction pattern of a (111) oriented RhSi single crystal superposed with a theoretically simulated pattern. Inset shows picture of the grown RhSi single crystal.	24
3.9	Refractive index (a) The real and imaginary parts of the refractive index. (b) The real and imaginary parts of the complex dielectric function.	26
3.10	Ideal conductivity (a) Here we compare the ideal Γ and R band conductivity, $\sigma_{1,\Gamma R}$, with the total conductivity of RhSi, σ_1 . (b) The fraction of σ_1 which constitutes the ideal Weyl conductivity.	28
3.11	Material properties (a) Power absorption coefficient α . (b) Fresnel transmission coefficient magnitudes $ t_s $ and $ t_p $. (c) Angle of refraction for incident angle $\theta_i = 45^\circ$. (d) Pump pulse length T estimated from the emitted terahertz waveforms.	29
3.12	Surface THz transmission and collection filter (a) Fraction of terahertz radiation transmitted from bulk into free space, determined by dc conductivity and optical conductivity measurements. (b) Fraction of terahertz collected and collimated by the OAP.	31
3.13	Filter calculation geometry (a) Illustration of photoexcited current at off-normal incidence. The pump light (red shading) is cast onto the sample which excites a current (orange shading). There is a time delay across the photoexcited region which affects the radiated angle, as in a phased array antenna. (b) Illustration of the polar coordinate system used in the filter calculation.	33
4.1	RhSi Crystal Structure (a) Unit cell displayed with the (111) direction pointing out of the page, showing the three-fold rotational symmetry of the crystal. (b) Extended RhSi structure, showing two alternate unit cells offset by $(1/2, 0, 1/2)$. When the unit cell marked by the orange frame is rotated 180° about the z axis, it is identical to the unit cell marked by the black frame, illustrating the two-fold screw symmetry.	37
4.2	Bulk CPGE Symmetry When circularly polarized light is incident on RhSi, the bulk CPGE current will be directed perpendicular to the surface, with its sign determined by the incident light's handedness. L and R refer to left- and right-handed circular polarization and \mathbf{j}_b refers to the bulk CPGE current.	39

4.3	Experimental Diagram for surface currents (a) Schematic of experiment used to detect photogalvanic currents in RhSi via terahertz detection. Near infrared (NIR) light with tunable wavelength and polarization is focused onto the (001) RhSi surface at normal incidence. Terahertz radiation is collected and collimated using off-axis parabolic mirrors. It passes through a wire-grid polarizer before being focused onto a ZnTe crystal. Light with $\lambda = 800$ nm and variable time delay Δt copropagates through the ZnTe for electro-optical detection of the terahertz. PD, photodiode; WP, Wollaston prism; WGP wire grid polarizer; $\lambda/2$, half-wave plate; $\lambda/4$, quarter-wave plate. (b) In one experimental configuration, the sample is kept fixed while the pump polarization is rotated by angle θ . The sample axes are set such that [100] and [010] are horizontal and vertical in the lab frame respectively. (c) In the second configuration, the pump polarization is fixed at $\theta = 0$ and the sample is rotated by and angle ϕ	40
4.4	Laue Diffraction Pattern Laue diffraction measurement overlaid with the predicted diffraction peaks of the 001 surface of space group 198.	41
4.5	CPGE on (001) (a) Amplitude of CPGE for horizontally and vertically polarized THz emission as a function of sample orientation ϕ . (b) Schematic showing directions of bulk PGE (\mathbf{j}_b , red) and surface PGE (\mathbf{j}_s , green) with normally incident light on the 001 surface of RhSi with the resulting radiation patterns. In general \mathbf{j}_s has components in x and y	43
4.6	Helicoid Surface Bands Schematic of surface helicoid bands including a photoexcitation of an electron at energy $\hbar\omega$ (red arrow) and the induced current (green arrow).	44
4.7	CPGE spectrum on (001) (a) CPGE spectral data for β_{xz} and β_{yz} compared with theory from Ref. [13]. (b) Experimental data compared with theory after rescaling of energy. Rescaling of the energy by a factor 1.25 is seen when DFT/LDA theory is augmented by inclusion of a certain amount of Hartree-Fock exchange using hybrid density functionals, for example in the Heyd, Scuseria, and Ernzerhof (HSE) approach.	45
4.8	LPGE on (001) (a) Terahertz amplitude along x and y as a function of linear pump polarization angle θ for $\lambda = 2000$ nm. (b) Results of fitting data in (a) to general LPGE tensor γ_{ijk}	46
4.9	Full LPGE scans on (001) LPGE measurements on RhSi 001 surface as a function of pump polarization angle for x and y components of terahertz. . . .	47
4.10	AFM Four AFM measurements on RhSi (001) surface showing crystal topography.	48

List of Tables

4.1	Room temperature single crystal Refinement result for RhSi.	42
-----	---	----

Acknowledgments

I'd like to thank my advisor Joe Orenstein for guiding me through graduate school and training me to conduct experiments, analyze results, effectively communicate findings, and everything else that is necessary to conduct scientific research. I could always count on you to have honest and shrewd feedback about my work and show investment in the results which is vital to any scientist in training.

I also want to thank Darius Torchinsky for being a very knowledgeable, hard working, and friendly collaborator. I learned a lot from you about physics and conducting research and am grateful to have worked with you.

While not directly involved in my graduate career, I'd also like to thank my undergraduate advisor Stuart Brown and mentor Adriane Steinacker for guiding me and encouraging me to continue in physics.

Thanks also to Liang Wu, Shreyas Patankar, and Arielle Little for training me in optics and helping me become an independent laser operator and experiment builder.

Thanks to Eric Thewalt, Liang Wu, Shreyas Patankar, Arielle Little, Ankit Kumar, Changmin Lee, Yue Sun, Veronika Sunko, and Elizabeth Donoway for all the good times working in lab together and having lunch on the patio.

I have also had many great times with Vir Bulchandani, Sam Ciocys, and Shawn Beckman throughout grad school and hope they continue well beyond it.

Thank you to Alex for your support and for always being there with me.

Thank you to my brother Wyatt and my parents Jeri and Robert for always being supportive and for raising me with such care.

Chapter 1

Berry Curvature and Weyl Semimetals

1.1 Berry curvature

Assume we have a system with a Hamiltonian that depends on a vector parameter \mathbf{k} : $H(\mathbf{k})$. In general \mathbf{k} can represent any physical quantity, such as magnetic field strength for example, but we will focus on the case of crystals, where \mathbf{k} will represent the momentum in reciprocal space. For each \mathbf{k} , the Hamiltonian has a set of eigenstates and energies

$$H(\mathbf{k})|n(\mathbf{k})\rangle = \varepsilon_n|n(\mathbf{k})\rangle. \quad (1.1)$$

We can consider what happens to the system if $\mathbf{k}(t)$ varies slowly over time. If the state at $t = 0$ is $|n(\mathbf{k}(0))\rangle$, then the system will stay in the n -th eigenstate, but will pick up an overall phase as follows [6, 36, 67]

$$|\psi_n(t)\rangle = e^{i\gamma_n(t)} \exp\left(-\frac{i}{\hbar} \int_0^t dt' \varepsilon_n(\mathbf{k}(t'))\right) |n(\mathbf{k}(t))\rangle. \quad (1.2)$$

The second phase factor is the dynamical phase as is present in any physical state. The first phase, $\gamma_n(t)$, is left for us to solve and without loss of generality we set $\gamma_n(0) = 0$ so that $|\psi_n(0)\rangle = |n(\mathbf{k}(0))\rangle$. To find this phase, we can insert Eq. 1.2 into the time-dependent Schrödinger equation:

$$i\hbar \frac{\partial}{\partial t} |\psi_n(t)\rangle = H(\mathbf{k}(t)) |\psi_n(t)\rangle. \quad (1.3)$$

This gives us

$$i\hbar \left[i \frac{\partial \gamma_n(t)}{\partial t} - \frac{i}{\hbar} \varepsilon_n(\mathbf{k}(t)) \right] |n(\mathbf{k}(t))\rangle + i\hbar \frac{\partial}{\partial \mathbf{k}} |n(\mathbf{k}(t))\rangle \cdot \frac{\partial \mathbf{k}}{\partial t} = \varepsilon_n(\mathbf{k}(t)) |n(\mathbf{k}(t))\rangle \quad (1.4)$$

Applying $\langle n(\mathbf{k}(t))|$ to the left side of each equation yields

$$i\hbar \left[i \frac{\partial \gamma_n(t)}{\partial t} - \frac{i}{\hbar} \varepsilon_n(\mathbf{k}(t)) \right] + i\hbar \langle n(\mathbf{k}(t))| \frac{\partial}{\partial \mathbf{k}} |n(\mathbf{k}(t))\rangle \cdot \frac{\partial \mathbf{k}}{\partial t} = \varepsilon_n(\mathbf{k}(t)) \quad (1.5)$$

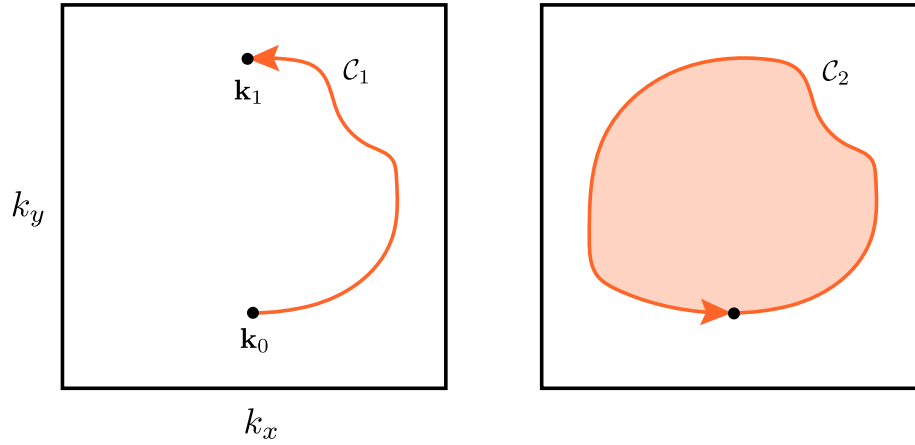


Figure 1.1: **Berry phase paths** Two paths in \mathbf{k} -space which will yield different Berry phases. Open paths (left) result in gauge-dependent Berry phases. Closed paths (right) result in gauge-*independent* Berry phases.

Simplifying gives

$$\frac{\partial \gamma_n(t)}{\partial t} = i \langle n(\mathbf{k}(t)) | \frac{\partial}{\partial \mathbf{k}} | n(\mathbf{k}(t)) \rangle \cdot \frac{\partial \mathbf{k}}{\partial t}. \quad (1.6)$$

Integrating over time yields

$$\gamma_n = \int_{\mathcal{C}} \mathcal{A}_n(\mathbf{k}) \cdot d\mathbf{k} \quad (1.7)$$

where

$$\mathcal{A}_n(\mathbf{k}) = i \langle n(\mathbf{k}) | \frac{\partial}{\partial \mathbf{k}} | n(\mathbf{k}) \rangle \quad (1.8)$$

and \mathcal{C} represents the curve traveled in \mathbf{k} -space up to time t . The quantity $\mathcal{A}_n(\mathbf{k})$ is referred to as the Berry connection or Berry potential.

Note that $\mathcal{A}_n(\mathbf{k})$ is not gauge-independent. If we add a \mathbf{k} -dependent phase $e^{i\phi(\mathbf{k})}$ to the states such that our new states are $e^{i\phi(\mathbf{k})} | n(\mathbf{k}) \rangle$, the Berry potential transforms as

$$\mathcal{A}_n(\mathbf{k}) \xrightarrow{\phi(\mathbf{k})} \mathcal{A}_n(\mathbf{k}) - \frac{\partial \phi}{\partial \mathbf{k}}. \quad (1.9)$$

Now let's consider what this gauge dependence means. For a path that is open ended, like \mathcal{C}_1 in Fig 1.1, the Berry phase γ_n will also be gauge-dependent and therefore not an observable quantity. It will transform as

$$\gamma_n(\mathbf{k}) \xrightarrow{\phi(\mathbf{k})} \gamma_n(\mathbf{k}) + \phi(\mathbf{k}_1) - \phi(\mathbf{k}_0). \quad (1.10)$$

For a closed curve, like \mathcal{C}_2 in Fig 1.1, $\mathbf{k}_0 = \mathbf{k}_1$, so the Berry phase is gauge-invariant and thus an observable quantity.

If we look back at Eq. 1.7, using Stokes' theorem we can transform this into the integral

$$\gamma_n = \int_S \boldsymbol{\Omega}_n(\mathbf{k}) \cdot d\mathbf{S} \quad (1.11)$$

where $\boldsymbol{\Omega}_n(\mathbf{k}) = \nabla_{\mathbf{k}} \times \mathcal{A}_n(\mathbf{k})$ is referred to as the Berry curvature and \mathcal{S} represents any surface that has \mathcal{C} as its boundary. This equation is now only valid when \mathcal{C} is a closed curve.

We can see easily that $\boldsymbol{\Omega}_n(\mathbf{k})$ is gauge invariant. Under a phase $\phi(\mathbf{k})$, the Berry curvature transforms as

$$\begin{aligned} \boldsymbol{\Omega}_n(\mathbf{k}) &\xrightarrow{\phi(\mathbf{k})} \nabla_{\mathbf{k}} \times (\mathcal{A}_n(\mathbf{k}) - \nabla_{\mathbf{k}}\phi) \\ &= \boldsymbol{\Omega}_n(\mathbf{k}) - \nabla_{\mathbf{k}} \times \nabla_{\mathbf{k}}\phi \\ &= \boldsymbol{\Omega}_n(\mathbf{k}) \end{aligned} \quad (1.12)$$

Since we know $\boldsymbol{\Omega}_n(\mathbf{k})$ is an observable quantity, we can ask what consequences it has on a crystal. One of the most direct cases is that an electron in a crystal with nonzero Berry curvature under an applied electric field \mathbf{E} will experience what is called an anomalous velocity [67]. The velocity of an electron at \mathbf{k} in the n -th band is

$$\mathbf{v}_n(\mathbf{k}) = \frac{1}{\hbar} \frac{\partial \varepsilon_n(\mathbf{k})}{\partial \mathbf{k}} - \frac{e}{\hbar} \mathbf{E} \times \boldsymbol{\Omega}_n(\mathbf{k}). \quad (1.13)$$

The first term is the normal band velocity, and the second term introduces a velocity that is perpendicular to the electric field. This contributes to the anomalous Hall effect.

The Berry curvature can be considered analogous to a magnetic field in reciprocal space. Just like a magnetic field, it is gauge-independent and can be written as the curl of a vector potential, $\mathcal{A}_n(\mathbf{k})$, which is gauge dependent.

Berry curvature under inversion and time reversal symmetries

We can ask what constraints, if any, inversion and time reversal symmetry will enforce on the Berry curvature. Applying the inversion operator to each side of the equation

$$\boldsymbol{\Omega}_n(\mathbf{k}) = \nabla_{\mathbf{k}} \times i \langle n(\mathbf{k}) | \frac{\partial}{\partial \mathbf{k}} | n(\mathbf{k}) \rangle \quad (1.14)$$

yields

$$\boldsymbol{\Omega}_n(-\mathbf{k}) = (-\nabla_{\mathbf{k}}) \times i \langle n(-\mathbf{k}) | (-\frac{\partial}{\partial \mathbf{k}}) | n(-\mathbf{k}) \rangle. \quad (1.15)$$

If the system under question is inversion-symmetric, then $|n(-\mathbf{k})\rangle = |n(\mathbf{k})\rangle$ and we find that

$$\boldsymbol{\Omega}_n(-\mathbf{k}) = \boldsymbol{\Omega}_n(\mathbf{k}). \quad (1.16)$$

Now apply the time reversal operator on Eq. 1.14:

$$\boldsymbol{\Omega}_n(-\mathbf{k}) = (-\nabla_{\mathbf{k}}) \times (-i) \langle n(-\mathbf{k}) | (-\frac{\partial}{\partial \mathbf{k}}) | n(-\mathbf{k}) \rangle. \quad (1.17)$$

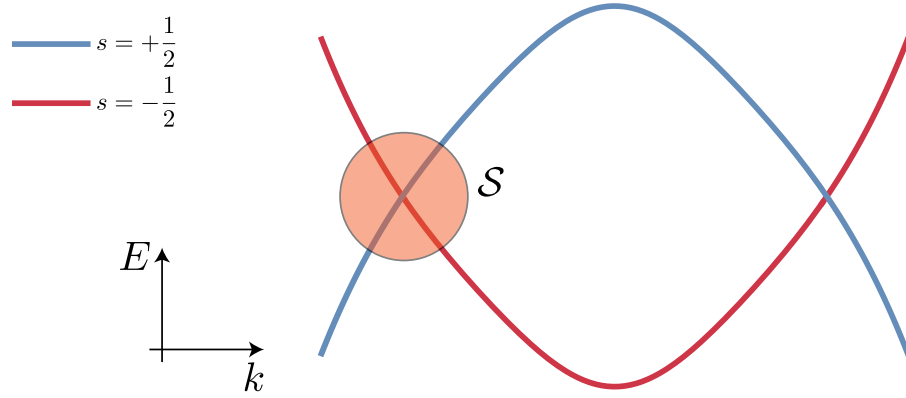


Figure 1.2: **Basic Weyl semimetal model** A basic model of a Weyl semimetal. There are two nodes with opposite signs as in Eq. 1.19. Integration of the Berry flux through the surface \mathcal{S} will yield the Chern number of the first Weyl node, as in Eq. 1.23.

We find that

$$\Omega_n(-\mathbf{k}) = -\Omega_n(\mathbf{k}). \quad (1.18)$$

Since Eqs. 1.16 and 1.18 are opposite constraints, a material must break either inversion or time-reversal symmetry (or both) to have nonzero Berry curvature.

1.2 Weyl Semimetals

A Weyl semimetal is a material with a Hamiltonian of the form

$$H = \pm \hbar v_F \mathbf{k} \cdot \boldsymbol{\sigma} \quad (1.19)$$

where

$$\boldsymbol{\sigma} = (\sigma_x, \sigma_y, \sigma_z) \quad (1.20)$$

is the Pauli matrix vector with

$$\begin{aligned} \sigma_x &= \begin{pmatrix} 0 & 1 \\ 1 & 0 \end{pmatrix} \\ \sigma_y &= \begin{pmatrix} 0 & -i \\ i & 0 \end{pmatrix} \\ \sigma_z &= \begin{pmatrix} 1 & 0 \\ 0 & -1 \end{pmatrix}. \end{aligned} \quad (1.21)$$

A band crossing occurs at $\mathbf{k} = 0$, and the Berry curvature can be written as

$$\Omega_n(\mathbf{k}) = \pm \frac{\mathbf{k}}{2k^3}. \quad (1.22)$$

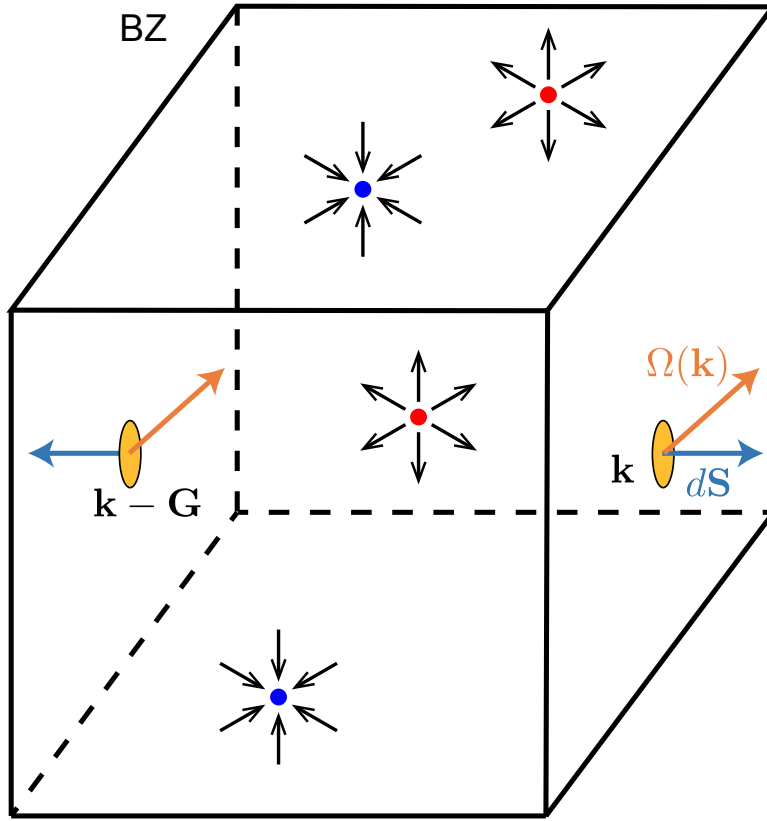


Figure 1.3: **Berry curvature in the Brillouin zone** The total Chern number of all Weyl nodes in the Brillouin zone must be zero. This can be seen by the fact that the total Berry flux through the Brillouin zone boundary must be zero.

This is mathematically identical to the electric field from a point charge, meaning that unlike with magnetic fields in real space, we can have Berry curvature monopoles in reciprocal space. The location of the Berry monopole is at the band crossing point, $\mathbf{k} = 0$, and is also called a Weyl node. We can define the charge, also called the Chern number, of a Berry monopole as

$$C = \frac{1}{2\pi} \int_{\mathcal{S}} \boldsymbol{\Omega}_n(\mathbf{k}) \cdot d\mathbf{S} = \pm 1 \quad (1.23)$$

where \mathcal{S} is a surface that encloses the point $\mathbf{k} = 0$. The sign of the Chern number also gives the chirality of the Weyl node. Fig. 1.2 shows a basic 1D model of a Weyl semimetal with two nodes of opposite Chern numbers. An example of a surface \mathcal{S} with nonzero Berry flux is shown.

One restriction to Weyl semimetals is that the total Chern number of all nodes in the

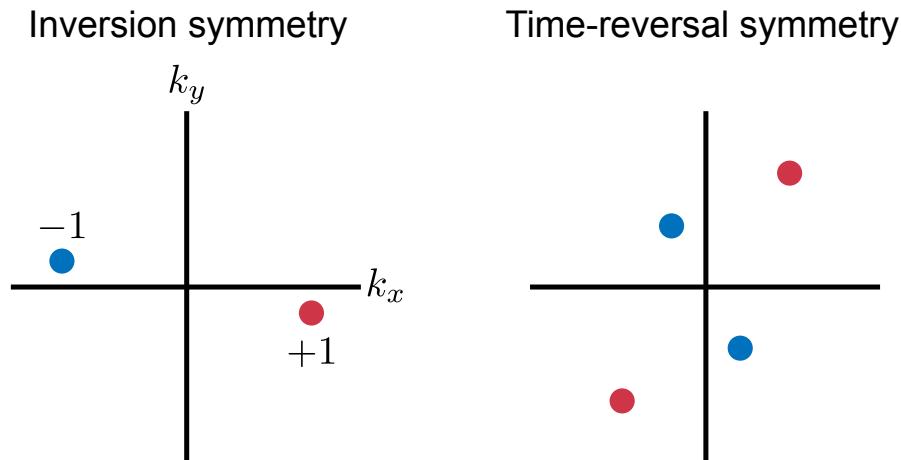


Figure 1.4: **Weyl node symmetries** Under inversion symmetry, the existence of a Weyl node at \mathbf{k} implies the existence of a Weyl node at $-\mathbf{k}$ with opposite Chern number. Under time-reversal symmetry, the existence of a Weyl node at \mathbf{k} implies the existence of a Weyl node at $-\mathbf{k}$ with the same Chern number.

Brillouin zone must be zero. We can prove this as follows. Assume you have some Brillouin zone with Berry curvature $\Omega(\mathbf{k})$. To find the total Chern number of all Weyl nodes, we must integrate as in Eq. 1.23 and pick our surface \mathcal{S} to be the boundary of the Brillouin zone. At some point \mathbf{k} on \mathcal{S} , there will be a Berry curvature $\Omega(\mathbf{k})$. If \mathbf{G} is a reciprocal lattice vector, then $\mathbf{k} - \mathbf{G}$ is also on the Brillouin zone boundary with the same Berry curvature, but the local surface normal vector $d\mathbf{S}$ will be opposite that of the point \mathbf{k} . Thus for every point on the Brillouin zone, there is another point which contributes equal and opposite Berry flux, and the total surface integral is zero. Fig. 1.3 illustrates this, showing various sources and sinks of Berry curvature represented by red and blue dots. This result can also be proven more formally, as shown by Nielsen and Ninomiya [49]. As a result of this constraint, Weyl nodes cannot be gapped independently and are thus topologically protected.

Let's consider the effects of symmetry on Weyl semimetals. As we already know, having a nonzero Berry curvature requires breaking at least one of inversion and time-reversal symmetry. This requirement applies equally to a material being a Weyl semimetal since a nonzero Berry curvature is a necessary feature.

If a material breaks time-reversal symmetry, but respects inversion symmetry, then $\Omega_n(-\mathbf{k}) = \Omega_n(\mathbf{k})$. This tells us that if there is a Weyl node at \mathbf{k} , there must be a Weyl node of the opposite Chern number at $-\mathbf{k}$. Conversely, if inversion symmetry is broken and time-reversal symmetry is respected then the Berry curvature must be odd. Thus if there is a Weyl node at \mathbf{k} , there must be another Weyl node with the same Chern number at $-\mathbf{k}$. This may seem counterintuitive, but note that it is the Berry curvature that is even and

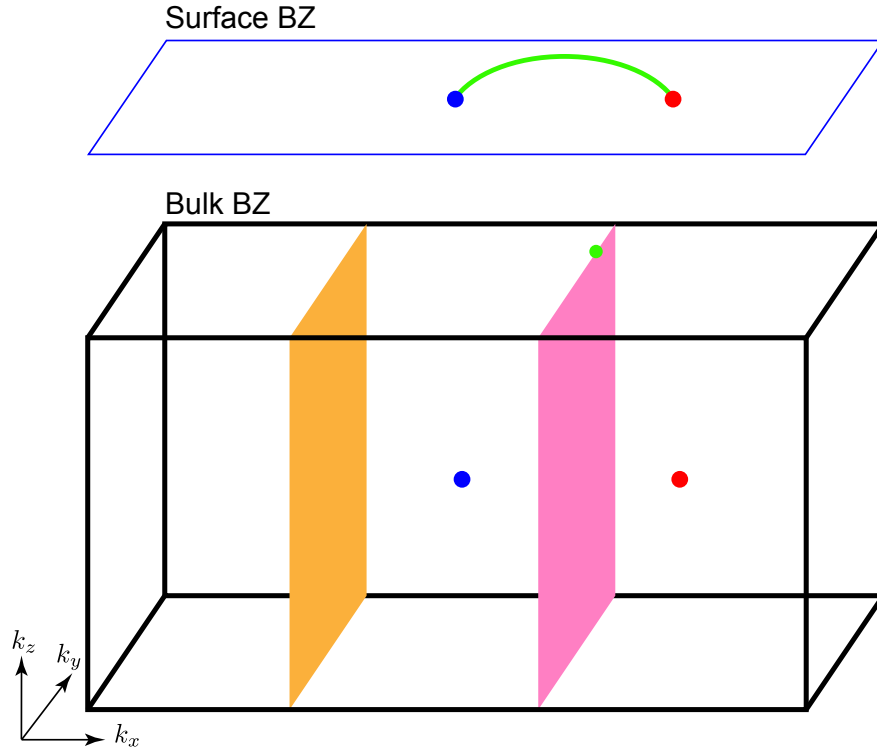


Figure 1.5: **Fermi arcs in Weyl semimetals** Weyl semimetals have surface states which connect the projections of the bulk Weyl points onto the surface Brillouin zone. This can be seen by considering the Berry flux through slices of the Brillouin zone between the nodes.

odd in these cases, not the Berry charge distribution which holds the opposite symmetry of $\Omega_n(-\mathbf{k})$. Due to the previous condition that the total Chern number of all Weyl nodes must be zero, this means there must be two more Weyl nodes of opposite Chern number elsewhere in the Brillouin zone for the time-reversal symmetric case¹. These two symmetry cases are illustrated schematically in Fig. 1.4.

Surface states in Weyl semimetals

Weyl nodes in a material necessitate the existence of surface states called Fermi arcs. We can see this using the following argument. If we take slices of the Brillouin zone, as is shown in Fig. 1.5, the slices can occur away from or between Weyl nodes of opposite charge. These slices form 2D systems and have 2D band structures. When they do not intersect a Weyl

¹There is an exception to this statement. If two nodes of opposite Chern number occur at time-reversal invariant momenta, then the minimum number of Weyl nodes is reduced to 2. One node can occur at Γ , and another of opposite charge at R in cubic Brillouin zones, for example. This is in fact the case for RhSi.

node they are gapped. When the Berry flux through them is nonzero, as with the right (pink) surface in Fig. 1.5, they then carry edge states at the Fermi energy [25, 65]. For each slice between the nodes, there is a surface state somewhere on the edge. By combining each of the edges of these slices, we form the collection of surface states called Fermi arcs which are open ended and begin and end at the projection of the Weyl nodes onto the surface Brillouin zone.

Chapter 2

Nonlinear Optics

2.1 Basic description

Nonlinear optical effects refer to processes in media where a polarization is induced by an externally applied electric field, often at optical frequencies, with a quadratic or higher power dependence. Mathematically this is written as follows. If a time-dependent electric field $\mathbf{E}(t)$ is applied to a medium, it will induce a polarization [7]

$$\mathbf{P}(t) = \epsilon_0 \left(\chi^{(1)} \mathbf{E}(t) + \chi^{(2)} \mathbf{E}(t) \mathbf{E}(t) + \chi^{(3)} \mathbf{E}(t) \mathbf{E}(t) \mathbf{E}(t) \dots \right) \quad (2.1)$$

where $\chi^{(n)}$ is a rank $n + 1$ tensor. We can write this using vector and tensor indices and Einstein notation as follows

$$P_i(t) = \epsilon_0 \left(\chi_{ij}^{(1)} E_j(t) + \chi_{ijk}^{(2)} E_j(t) E_k(t) + \chi_{ijkl}^{(3)} E_j(t) E_k(t) E_l(t) \dots \right) \quad (2.2)$$

For now we will assume $\epsilon_0 = 1$ for ease of notation. Individual terms on the right in the above equation can be referred to as $P_i^{(1)}(t)$, $P_i^{(2)}(t)$, etc. The first term on the right is related to the most commonly used optical properties like index of refraction n , optical conductivity σ , and the dielectric constant ϵ . $\chi_{ij}^{(1)}$ is called the linear susceptibility. The rest of the terms are nonlinear effects, named for the nonlinear dependence on $\mathbf{E}(t)$.

Inversion symmetry

Let us consider the properties of the tensors $\chi^{(n)}$ under inversion symmetry. Consider $P_i^{(1)} = \chi_{ij}^{(1)} E_j$, where we have dropped the explicit time dependence on P and E . If we apply the inversion operator to each side of this equation we get

$$-P_i^{(1)} = \chi_{ij}^{(1)} (-E_j) = -\chi_{ij}^{(1)} E_j. \quad (2.3)$$

We have learned nothing by doing this, thus there are no constraints on $\chi^{(1)}$ under inversion symmetry. Now do the same to the equation $P_i^{(2)} = \chi_{ijk}^{(2)} E_j E_k$, which gives us

$$-P_i^{(2)} = \chi_{ijk}^{(2)} (-E_j)(-E_k) = \chi_{ijk}^{(2)} E_j E_k. \quad (2.4)$$

This tells us that

$$P_i^{(2)} = -P_i^{(2)} = 0 \quad (2.5)$$

and therefore

$$\chi_{ijk}^{(2)} = 0. \quad (2.6)$$

Thus $\chi_{ijk}^{(2)}$ can only be nonzero in media that break inversion symmetry. In fact, we find that this is true for all even order nonlinear tensors $\chi^{(n)}$. For odd n , $\chi^{(n)}$ is allowed regardless of the spatial symmetry, although constraints may be placed on the relative components of the tensors depending on the space group. One example of this effect is that you cannot have birefringence (a property of $\chi_{ij}^{(1)}$ in materials with 4-fold rotational symmetry. In this work, we primarily measure properties related to $\chi_{ijk}^{(2)}$. Some linear properties are used to aid us in understanding our systems. For simplicity of notation, χ_{ijk} should be understood as the second order susceptibility $\chi_{ijk}^{(2)}$.

General symmetry constraints

For a general operator \mathcal{O} , the tensor χ_{ijk} transforms as

$$\chi'_{ijk} = \mathcal{O}_{i\alpha} \mathcal{O}_{j\beta} \mathcal{O}_{k\gamma} \chi_{\alpha\beta\gamma}. \quad (2.7)$$

\mathcal{O} can be, for example, a rotation, a mirror, or a combination of these. If \mathcal{O} is a symmetry of the system, then all properties are invariant under the transformation and therefore $\chi'_{ijk} = \chi_{ijk} = \mathcal{O}_{i\alpha} \mathcal{O}_{j\beta} \mathcal{O}_{k\gamma} \chi_{\alpha\beta\gamma}$ which allows us to find the constraints on χ_{ijk} if we know all the symmetries the material in question. RhSi is in space group 198 and thus has 2-fold screw symmetry about the x -axis, and a 3-fold rotational symmetry along the [111] direction. These two symmetry operators can be combined to form new symmetry operations. We will rely on these two symmetries along with the fact that RhSi has no mirror or improper rotational symmetries later on.

2.2 Frequency considerations in nonlinear optics

Consider an optical electric field at frequency ω ,

$$E(t) = E_0 e^{i\omega t} + c.c. \quad (2.8)$$

The second order polarization is thus

$$\begin{aligned} P^{(2)}(t) &= \chi^{(2)} E(t) E(t) \\ &= \chi^{(2)} (|E_0|^2 + E_0^2 e^{2i\omega t} + c.c.). \end{aligned} \quad (2.9)$$

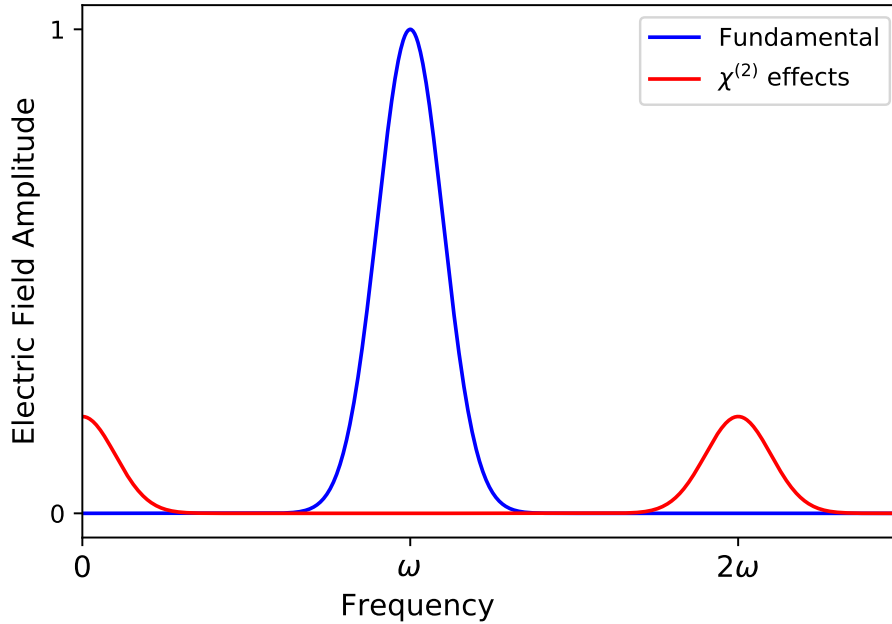


Figure 2.1: **Second order susceptibility spectrum** Schematic of fundamental and second order susceptibility within a material. Light with frequency centered around ω produces electric fields in the material at dc and 2ω . These two effects are referred to as the photogalvanic effect and second harmonic generation, respectively.

We now see there there is a time-independent (dc) second order polarization,

$$P_{dc} = \chi^{(2)} |E_0|^2 \quad (2.10)$$

and a time-dependent one,

$$P_{2\omega} = \chi^{(2)} (E_0^2 e^{2i\omega t} + c.c.). \quad (2.11)$$

This field has frequency 2ω , twice that of the original optical beam. This means that second order processes are comprised of two simultaneous effects, creation of a dc current, called the photogalvanic effect (PGE), and creation of an alternating field at twice the frequency of the fundamental light, referred to as second harmonic generation (SHG). These two effects are illustrated schematically in Fig. 2.1. Here, the spectrum of the fundamental light (blue curve) is a Gaussian centered at ω . This is the case for light originating from an ultrafast pulsed laser. Because of the temporal isolation of light into short pulses, the spectrum has some nonzero spread. This can be seen through a simple Fourier transformation of an ac signal at ω with a Gaussian envelope function. For a continuous wave laser, the spectrum would look like a Dirac delta function at ω , and second order processes would result in exactly dc currents and continuous wave light at exactly 2ω . The two effects are further illustrated in Fig. 2.2. In this work we will be focusing on the PGE.

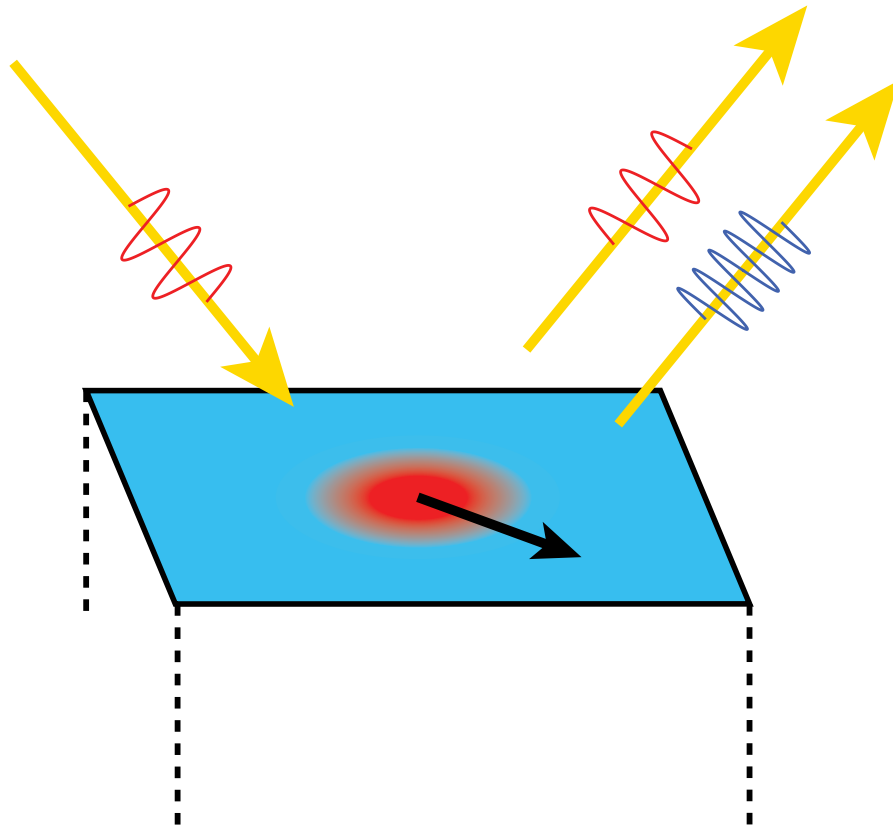


Figure 2.2: **Second order effects** Schematic of fundamental light striking a material and producing second order effects. SHG light is radiated from the material with twice the frequency and a photogalvanic current (black arrow) is produced. For fundamental light with some frequency spread $\Delta\omega$, the photogalvanic current will have a small frequency and thus radiate.

The difference of frequency between these two effects and the fundamental light makes distinguishing them from linear properties easy. For SHG, spectral filters allow for blocking of linear reflected light, so that we can isolate our detectors to light at 2ω . For a wide range of frequencies, we can use traditional silicon or similar semiconductor based detectors to measure the intensity of this light. We will later see that measurement of the PGE, which often comes in frequencies near 1 THz, will require a more specialized detection scheme.

Chapter 3

Bulk Photogalvanic Effects in RhSi

3.1 Photogalvanic effects and Weyl Semimetals

Photogalvanic effects, wherein photocurrents proportional to the light intensity appear in the absence of an applied bias, are examples of responses allowed by symmetry in Weyl semimetals that break inversion. In the circular photogalvanic effect (CPGE), the direction of the current reverses on changing the photon polarization between left and right circular [4]. The CPGE has been used effectively to probe broken symmetry states in a variety of condensed matter systems [2, 30, 21, 20].

The first hint that topology can shape the CPGE amplitude [26] arose in the context of the crossing of non-degenerate bands at the surface of 3D topological insulators such as Bi_2Se_3 . Fig. 3.1 illustrates how helicity-dependent photocurrent can arise in such a system as a result of the correlation of the direction of an electron's momentum with that of its spin (or pseudospin). A photon with definite helicity induces a transition that flips the direction of spin, and through spin-momentum locking creates a particle-hole pair that carries a net current. Hosur [26] showed that the current associated with photoexcitation of an electron-hole pair at momentum \mathbf{k} was proportional to the Berry curvature, $\mathbf{\Omega}(\mathbf{k})$. However, in this two-dimensional (2D) system the net CPGE current vanishes on integration over \mathbf{k} in the presence of n -fold rotational symmetry (for $n \geq 3$). Nonzero CPGE requires lowering the symmetry by in-plane strain, magnetic field, or inducing photoexcitation at oblique incidence [52].

Recently de Juan et al. [35] showed that, in contrast to the 2D case, rotational symmetry does not cause CPGE to vanish for the 3D bandcrossings that define Weyl semimetals. Instead, the CPGE current from a single Weyl node in the clean, non-interacting limit is proportional to its quantized topological charge and fundamental constants e and \hbar . In an ideal system, this result is independent of material-specific properties and the frequency of the excitation light over a band of wavelengths. The rate of current generation by circularly

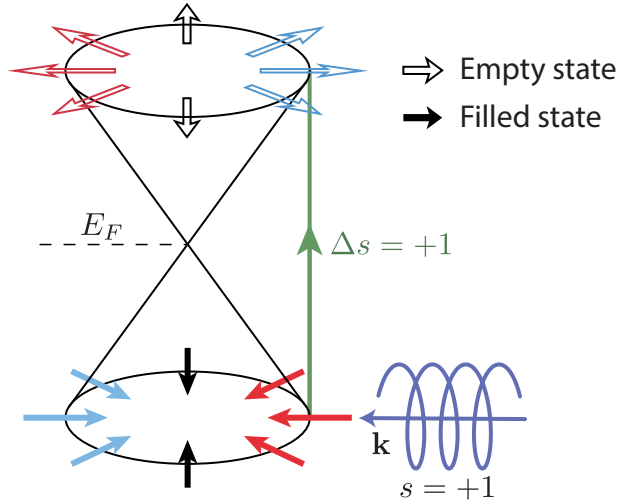


Figure 3.1: **Photocurrents from a Weyl node** Schematic illustrating selection rules for optical transitions on a Weyl node with circularly polarized photons. With photon spin $s = +1$ (-1), only transitions on the right (left) side of the node will be allowed, leading to an asymmetric excited state and thus a photocurrent.

polarized light is described by the equation,

$$\frac{dj_i}{dt} = i\pi \frac{e^3}{h^2} C \hat{\beta}_{ij} [\mathbf{E}(\omega) \times \mathbf{E}^*(\omega)]_j \quad (3.1)$$

where $\text{Tr} \hat{\beta}_{ij} = 1$ and C is the monopole charge (or Chern number) [35].

Although each Weyl node contributes a quantum of CPGE, this direct signature of topological charge is hidden in systems that retain mirror symmetry, which requires that nodes of opposite charge are degenerate in energy. This leads to an exact cancellation of the CPGE current for pairs of perfectly symmetric Weyl nodes. Despite this, nonzero CPGE is seen in mirror symmetric Weyl semimetals such as TaAs [43, 62, 60, 22, 31, 41] as a consequence of departures from symmetric dispersion that occur in real systems, for example curvature or tilting of the Dirac cones [10]. However, in such systems the CPGE amplitude is not a topological property uniquely related to the Berry monopole charge.

The properties of chiral Weyl semimetals, in which all mirror symmetries are broken, are qualitatively different from mirror preserving materials such as TaAs [35, 11]. In chiral structures, isolated Weyl nodes can occur at time-reversal invariant momenta. As a result, they can be separated by wavevectors on the order of the full Brillouin zone, allowing for a richer structure of Fermi arc surface states [8, 12, 64]. Of more direct relevance to the CPGE, in chiral Weyl semimetals nodes with opposite topological charge need not be degenerate in energy. Thus, it is possible for one node to lie near the Fermi energy, E_F , while its

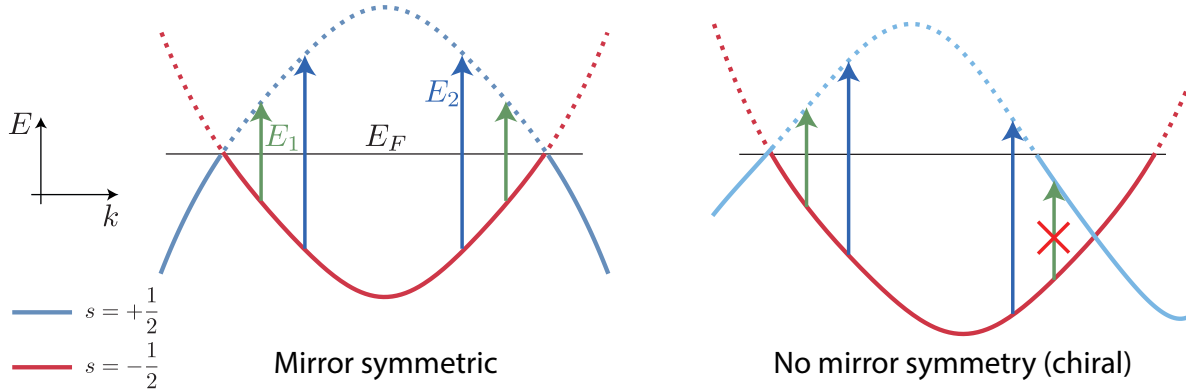


Figure 3.2: **Weyl nodes and mirror symmetry** When mirror symmetry is present, nodes of opposite chirality are degenerate, and thus produce equal and opposing CPGE contributions. In a chiral system, nodes can be degenerate and thus optical transitions near one node can be Pauli blocked, leaving the CPGE from the other node unopposed.

oppositely charged partner is below. Transitions near the node below E_F are Pauli blocked at sufficiently low photon energy, and a quantized CPGE (QCPGE) arising from the Weyl node near E_F will emerge. This is illustrated in Fig. 3.2. This prediction [35, 11] motivates measurements of CPGE as a function of photon energy to search for an energy window in which overall Berry charge neutrality is frustrated by Pauli blocking, even if the precise quantization suggested by Eq. 3.1 is modified by disorder or interaction effects.

Chiral semimetals can host multiple bandcrossings with monopole charges C larger than one. Despite higher multiplicity and band curvature in these multifold fermion systems, it was shown theoretically that approximate CPGE quantization continues to hold, with corrections at low energy when spin-orbit interaction is included [12, 17, 34]. Further, the magnitude of the CPGE is enhanced for multifold compared to Weyl fermions because of the greater topological charge.

RhSi is a structurally chiral material proposed as an ideal candidate to exhibit a QCPGE. The prediction of multifold fermion dispersion and exotic Fermi arcs [12, 64] was confirmed by ARPES measurements in this compound and in isostructural materials [57, 63, 58]. The CPGE is predicted to have an especially simple form in this family of compounds because in their cubic space group, $P2_13$ (#198), the dimensionless anisotropy tensor $\hat{\beta}_{ij}$ reduces to the unit tensor multiplied by a scalar $\beta = 1/3$. Further, band theory predicts a large energy splitting between the two nodes of opposite charge, such that the regime of Pauli blocking extends to a photon energy of approximately 0.65 eV, well into the near-infrared range [17].

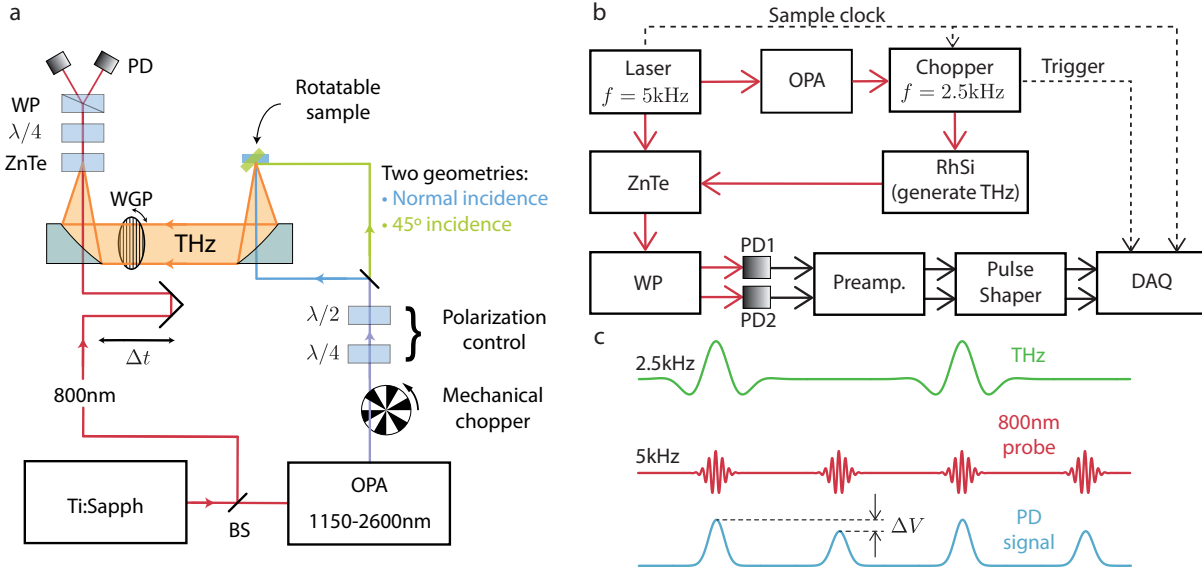


Figure 3.3: **Experimental apparatus** (a) Schematic of experiment showing optical paths and optical elements. PD, photodiode; BS, beam splitter; $\lambda/2$, half-wave plate; $\lambda/4$ quarter-wave plate; WP, Wollaston prism. (b) Schematic showing flow of optical paths (red lines) and electronic references (dashed black lines) and signals (black lines) resulting in the measured value for the terahertz electric field. (c) 800nm optical pulses arrive at the photodiode at 5kHz, while the terahertz pulses arrive at 2.5kHz due to the optical chopper blocking every other pulse in the pump arm of the experiment. This allows for direct comparison of the electro-optical effect in ZnTe with the terahertz signal present and not present. A particular time delay Δt is chosen before taking a single measurement which is done by averaging a certain number of pulses, typically in the range 5000–25000 depending on the signal strength and noise level.

3.2 Experimental setup

In order to test the prediction of CPGE from an isolated Weyl point in RhSi, a experiment requires control of incident photon energy across a region where transitions from one Weyl point are blocked and a region where transitions from both Weyl points are allowed. This allows for observation of the contrast between the two cases.

A schematic of the apparatus for photogeneration and detection of CPGE current in the photon energy range from 0.48 to 1.1 eV is shown in Fig. 3.3. The component of photogalvanic current parallel to the surface of the RhSi crystal radiates an electromagnetic pulse into free space that is focused onto a ZnTe crystal for time-resolved electro-optic sampling. This all-optical technique avoids artifacts from asymmetric electrical contacts and laser-induced heating, and enables precise determination the direction of the current

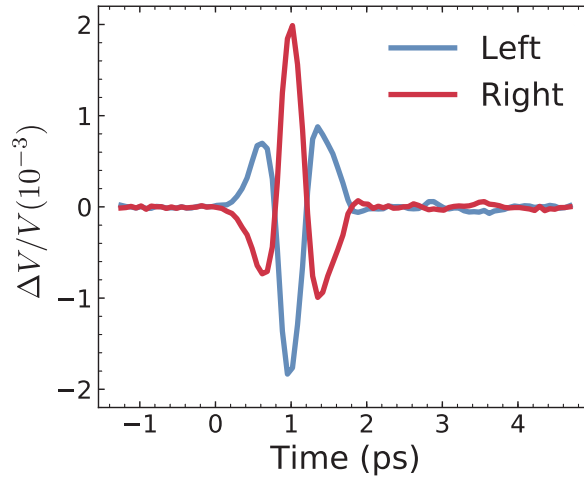


Figure 3.4: **Terahertz pulses** An example of terahertz pulses measured from RhSi using circularly polarized light at $\lambda = 2000\text{nm}$.

through measurement polarization of the pulse in the far-field. Fig. 3.4 shows typical pulses measured with excitation photon energy 0.60 eV. The reversal of polarity between left and right circular excitation is the defining property of the CPGE.

3.3 PGE Symmetry

Before examining the CPGE spectrum, we first tested that the CPGE and linear PGE (LPGE) currents obey the polarization properties consistent with the space group symmetry of RhSi. Because $\hat{\beta}_{ij}$ is predicted to be diagonal, the CPGE current should obey the relation, $\mathbf{j} \propto \beta(\mathbf{E} \times \mathbf{E}^*)$, and therefore be directed parallel to the wavevector of light, independent of the crystal orientation. The direction of the LPGE current, on the other hand, depends on both the light polarization and the crystal axes. For our measurements, in which the sample was rotated by an angle ϕ about the normal to the (111) surface, the direction of the LPGE surface current, θ , is predicted to rotate three times as fast, i.e. $\theta = 3\phi$. We can derive these statements about CPGE and LPGE as follows.

CPGE

For cubic space group $P2_13$ the only nonvanishing elements of σ_{ijk} have indices xyz and permutations. The elements with even permutations of xyz are equal to σ_{xyz} and odd permutations are equal to σ_{xyz}^* . If we write $\sigma_{xyz} = \alpha + i\gamma$ where α and γ are both real, the structure of the third rank tensor can be displayed in the form,

$$\sigma^{(2)} = \begin{pmatrix} \begin{pmatrix} 0 \\ 0 \\ 0 \end{pmatrix} & \begin{pmatrix} 0 \\ 0 \\ \alpha + i\gamma \end{pmatrix} & \begin{pmatrix} 0 \\ \alpha - i\gamma \\ 0 \end{pmatrix} \\ \begin{pmatrix} 0 \\ 0 \\ \alpha - i\gamma \end{pmatrix} & \begin{pmatrix} 0 \\ 0 \\ 0 \end{pmatrix} & \begin{pmatrix} \alpha + i\gamma \\ 0 \\ 0 \end{pmatrix} \\ \begin{pmatrix} 0 \\ \alpha + i\gamma \\ 0 \end{pmatrix} & \begin{pmatrix} \alpha - i\gamma \\ 0 \\ 0 \end{pmatrix} & \begin{pmatrix} 0 \\ 0 \\ 0 \end{pmatrix} \end{pmatrix} \quad (3.2)$$

where the element σ_{ijk} is the k th element of the column vector in the i th row and j th column of the matrix.

The circular photogalvanic current can be written in terms of the photon helicity,

$$\mathbf{j}_i \propto \beta_{ij} (\mathbf{E} \times \mathbf{E}^*)_j. \quad (3.3)$$

The second rank CPGE tensor is contracted from the third-rank conductivity tensor according to the relation,

$$\beta_{ij} = \sigma_{ikl} \epsilon_{jkl}, \quad (3.4)$$

where ϵ_{jkl} is the unit antisymmetric tensor. Substitution of the conductivity tensor for the RhSi space group (Eq. 3.2) yields,

$$\beta_{ij} = i\beta \delta_{ij}, \quad (3.5)$$

where δ_{ij} is the Kronecker delta. Substitution of β_{ij} into Eq. 3.3 yields,

$$\mathbf{j} \propto i\beta \mathbf{E} \times \mathbf{E}^*, \quad (3.6)$$

which shows that for the case of space group $P2_13$ the CPGE current is always directed parallel to the helicity vector, regardless of its direction with respect to the crystal axes.

LPGE

We use Rodrigues' rotation formula to transform Eq. 3.2 into the basis where z' is parallel to the (111) direction in the crystal basis, which yields

$$\sigma^{(2)} \propto \begin{pmatrix} \begin{pmatrix} -\alpha\sqrt{2} \\ 0 \\ -1 \end{pmatrix} & \begin{pmatrix} 0 \\ \alpha\sqrt{2} \\ i\gamma\sqrt{3} \end{pmatrix} & \begin{pmatrix} -\alpha \\ -i\gamma\sqrt{3} \\ 0 \end{pmatrix} \\ \begin{pmatrix} 0 \\ \alpha\sqrt{2} \\ -i\gamma\sqrt{3} \end{pmatrix} & \begin{pmatrix} \alpha\sqrt{2} \\ 0 \\ -\alpha \end{pmatrix} & \begin{pmatrix} \sqrt{3}\alpha \\ -\alpha \\ 0 \end{pmatrix} \\ \begin{pmatrix} -\alpha \\ i\gamma\sqrt{3} \\ 0 \end{pmatrix} & \begin{pmatrix} -\sqrt{3}\alpha \\ -\alpha \\ 0 \end{pmatrix} & \begin{pmatrix} 0 \\ 0 \\ 2\alpha \end{pmatrix} \end{pmatrix}. \quad (3.7)$$

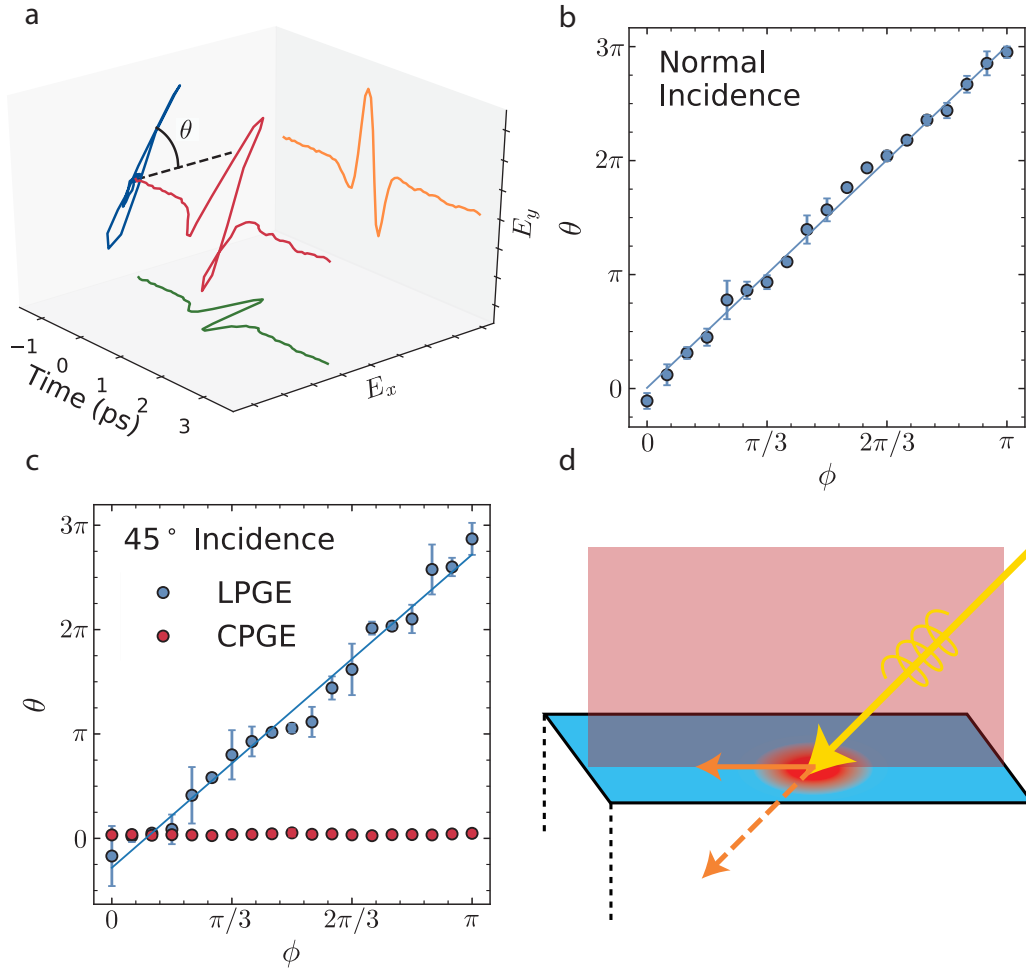


Figure 3.5: **Photocurrent symmetry** (a) Measurement of the THz polarization. Orange and green curves show the vertical and horizontal components of the pulse as a function of time. The reconstructed THz pulse (red curve) is then projected onto a plane, showing the direction of linear polarization, θ . (b) Dependence of the angle of LPGE terahertz polarization, θ , on angle of rotation of (111) face about the surface normal, ϕ , with pump at normal incidence. The relation $\theta = 3\phi$ predicted by the space group $P2_13$ symmetry is confirmed. The CPGE signal is below measurement noise level in this geometry. (c) Same as (b) except for 45° incidence. LPGE polarization again varies as $\theta = 3\phi$. CPGE is horizontally polarized independent of the crystal orientation confirming that the CPGE current is parallel to the pump wavevector. (d) Schematic showing that the resulting in plane CPGE current is fixed by the plane of incidence of the pump light. The CPGE current at normal incidence is normal to the surface of the sample and thus does not radiate into free space.

Using this tensor we can calculate the LPGE response for fixed linear pump polarization as the crystal is rotated about the z' (or (111)) axis by an angle ϕ . The crystal rotation corresponds to the transformation $\sigma'_{\alpha\beta\gamma} = R_{\alpha i}(\phi)R_{\beta j}(\phi)R_{\gamma k}(\phi)\sigma_{ijk}$, where,

$$R(\phi) = \begin{pmatrix} \cos(\phi) & \sin(\phi) & 0 \\ -\sin(\phi) & \cos(\phi) & 0 \\ 0 & 0 & 1 \end{pmatrix}. \quad (3.8)$$

If the pump polarization is fixed in the x' direction, then the LPGE current depends only on the tensor elements σ'_{xxx} and σ'_{yxx} and from Eqs. 3.7 and 3.8 we have,

$$\begin{aligned} \sigma'_{xxx} &= R_{xx}^3\sigma_{xxx} + R_{xx}R_{xy}^2\sigma_{xyy} + R_{xy}R_{xx}R_{xy}\sigma_{yxy} + R_{xy}^2R_{xx}\sigma_{yyx} \\ &\propto \left(-\sqrt{2}\cos^3(\phi) + 3\sqrt{2}\cos\phi\sin^2\phi \right) \\ &= -\sqrt{2}\cos(3\phi) \end{aligned} \quad (3.9)$$

and

$$\begin{aligned} \sigma'_{yxx} &= R_{yx}R_{xx}^2\sigma_{yxy} + R_{yx}R_{xy}^2\sigma_{xyy} + R_{yy}R_{xx}R_{xy}\sigma_{yxy} + R_{yy}R_{xy}R_{xx}\sigma_{yyx} \\ &\propto \left(-3\sqrt{2}\cos^2\phi\sin\phi - \sqrt{2}\sin^3\phi \right) \\ &= \sqrt{2}\sin(3\phi). \end{aligned} \quad (3.10)$$

From Eqs. 9 and 10 we obtain the dependence of the LPGE current on crystal rotation angle,

$$\mathbf{j}(\phi) \propto \cos(3\phi)\hat{\mathbf{x}}' - \sin(3\phi)\hat{\mathbf{y}}'. \quad (3.11)$$

Eq. 3.11 implies that the angle, θ , of the LPGE current relative to the x' axis is given by $\theta = 3\phi$.

Results

Fig. 3.5(a) shows a typical measurement of the direction of the current, obtained by using a linear polarizer to resolve the two orthogonal components of the electric field. Fig. 3.5(b) shows the direction of the LPGE current as a function of ϕ for normal incidence, confirming the relation $\theta = 3\phi$. In contrast, the CPGE signal is below measurement noise level at normal incidence, consistent with the prediction that it flows directly into the bulk of the crystal, with zero surface component and thus no measurable radiation. At 45° incidence (Fig. 3.5(c)), the LPGE current exhibits the same $\theta = 3\phi$ dependence and CPGE current is now observed, with direction fixed to be horizontal and independent of ϕ . This latter result is consistent with the expectation that the CPGE current is parallel to the wavevector of the excitation light, because in this case the surface current direction is locked to the plane of incidence (see Fig. 3.5(d)), independent of crystal orientation.

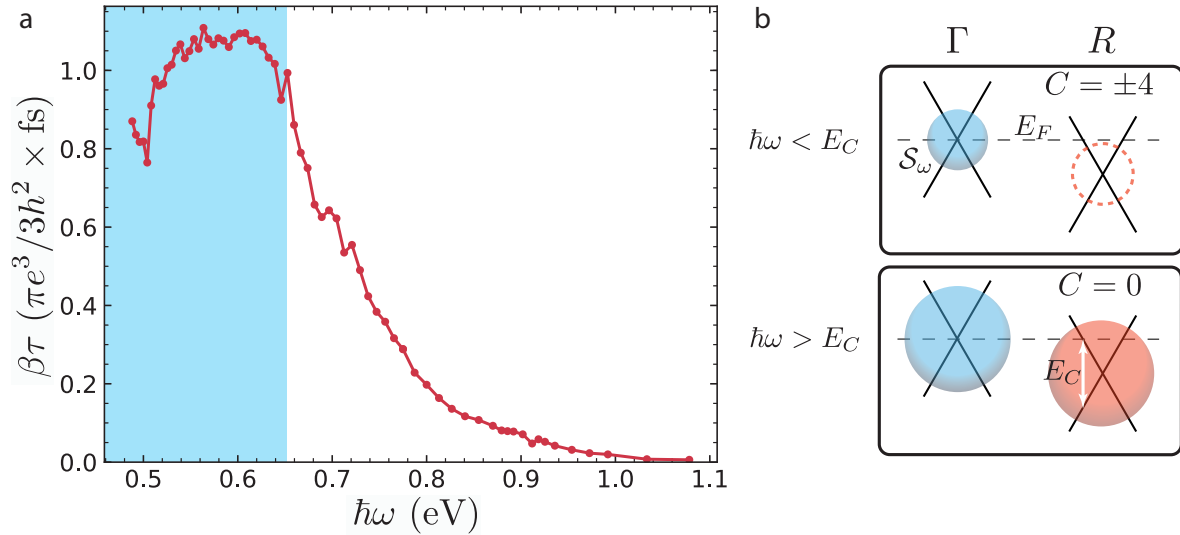


Figure 3.6: **CPGE spectrum** (a) CPGE amplitude $\beta\tau$ in units of $\frac{\pi e^3}{3h^2} \times \text{fs}$ as a function photon energy, showing abrupt quenching above 0.65 eV. (b) Schematic showing the surface \mathcal{S}_ω in k -space defined by the available optical transitions at photon energy $\hbar\omega$. For $\hbar\omega < E_C$, \mathcal{S}_ω encloses a single node and has integrated Berry flux $C = \pm 4$. Above E_C it encloses two topological nodes of opposite chirality and $C = 0$. The blue shaded region in (a) indicates the region where \mathcal{S}_ω encloses only a single node.

3.4 CPGE Spectrum

Having confirmed that the polarization selection rules are consistent with crystal symmetry, we turn to the dependence of the CPGE amplitude on photon energy $\hbar\omega$ in the range from 0.5 to 1.1 eV. We note first that this amplitude is proportional to the $\beta\tau$ product, where τ is the momentum lifetime of photexcited carriers, rather than β itself. The reason is that the dynamics are in the quasi-steady state regime of Eq. 3.1, in which τ is shorter than the ~ 100 fs duration of the excitation pulse. This conclusion follows from the observation that the THz emission waveform follows the envelope of the laser pulse, rather than persisting for an observable momentum lifetime. The quasi-steady state regime is consistent with $\tau = 8$ fs for equilibrium carriers as determined from transport measurements (see Section 3.5). The τ of photoinjected “hot” carriers can be expected to be at least as short as that of the equilibrium ones.

Fig. 3.6(a) shows the dependence of $\beta\tau$ on pump photon energy. Converting the measured THz emission to surface current and ultimately an absolute determination of $\beta\tau$ requires accounting for multiple wavelength-dependent factors involving the photoexcitation source, the linear optical response of RhSi at the pump laser and THz wavelengths, and the spectral function of the THz detection optics. Propagation of systematic and statistical errors through

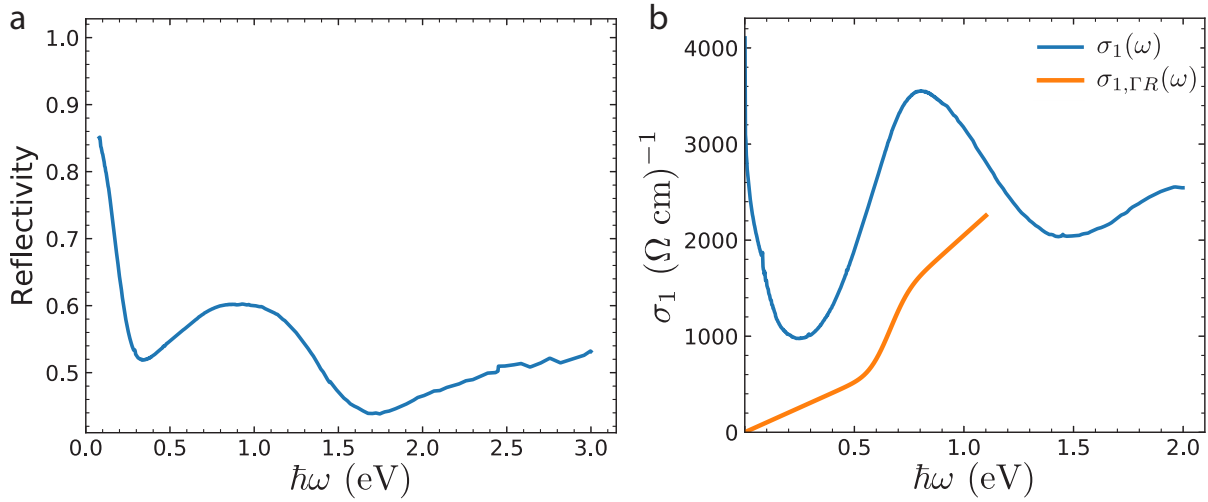


Figure 3.7: **Reflectivity and optical conductivity** (a) Measured reflectivity of RhSi. (b) Optical conductivity determined by reflectivity measurements and Kramers-Kronig analysis (blue curve). The Drude peak is used to infer that the scattering time has value $\tau = 8.6$ fs. The orange curve represents the optical conductivity from the Γ and R nodes alone [56].

these multiple factors suggests an order of magnitude uncertainty in the absolute surface current.

The striking feature of the CPGE spectrum is the rapid decrease in $\beta\tau$ that occurs when $\hbar\omega$ exceeds 0.65 eV. Above this energy, $\beta\tau$ decays from its peak value by a factor of ~ 200 as $\hbar\omega$ reaches 1.1 eV. This spectral feature cannot be accounted for by the aforementioned wavelength-dependent conversion factors, as they vary smoothly through this energy range.

The photon energy at which the CPGE response decreases agrees with theoretical predictions [17, 34] based on a crossover in effective Berry monopole charge as a function of $\hbar\omega$. Fig. 3.6(b) illustrates this crossover, showing the evolution of the surface \mathcal{S}_ω in \mathbf{k} -space defined by the momenta where there are available optical transitions at energy $\hbar\omega$. The CPGE is proportional to the integrated flux of the Berry curvature through \mathcal{S}_ω [35], referred to as C . For sufficiently small $\hbar\omega$, \mathcal{S}_ω is a single surface enclosing the Γ -point and the total Berry flux is equal to the topological charge at Γ , which is 4. For $\hbar\omega > E_C$ a surface surrounding the R -point appears such that \mathcal{S}_ω now encloses two nodes of opposite chirality, driving the net Berry flux, and consequently the CPGE, to zero.

Although our observation of the predicted cutoff in the CPGE spectrum is suggestive of an interpretation in terms of bandstructure topology, this tentative assignment comes with several caveats. First, the photon-energy dependence of the hot carrier lifetime will be reflected in the CPGE response, which as previously mentioned, is proportional to the $\beta\tau$ product. Although we cannot measure $\tau(\omega)$ directly as it is below our ~ 100 fs time resolution,

we believe that it is unlikely to decrease sufficiently rapidly with energy to account for the ~ 100 -fold decrease in the CPGE response that begins when $\hbar\omega$ exceeds 0.65 eV. This would require that τ decrease from its “cold carrier” value of 8 fs to ~ 0.08 fs. Converting τ to mean-free path l using the Fermi velocity $v_F \approx 4.3 \times 10^7$ cm/s derived from DFT bandstructure [12] yields $l \approx 3.5$ nm, or about seven lattice constants, for electrons at the Fermi surface. Thus l would have to decrease to less than 0.1 lattice constant to account for the entire decrease in CPGE current as the photon energy is increased. Nevertheless, it is certainly possible that the energy dependence of τ contributes to the observed CPGE photocurrent spectrum.

A further consideration for the interpretation of the CPGE spectrum is the possibility that optical transitions, other than those originating from the Γ and R points, contribute to photon absorption in the infrared range. To examine this possibility we measured the linear optical conductivity, $\sigma_1(\omega)$, throughout the spectral range of our photocurrent spectroscopy. Figs. 3.7(a) and (b) show the normal incidence reflectivity measured at room temperature and the corresponding $\sigma_1(\omega)$ obtained by Kramers-Kronig analysis, respectively. Shown in Fig. 3.7(b) as well is the predicted contribution from interband transitions near the Weyl nodes [56], where the spectrum is smoothed assuming disorder and thermal broadening to be ~ 0.1 eV. From the comparison we see that $\sigma_1(\omega)$ does indeed show contributions beyond those expected from interband transitions near the Weyl nodes: a Drude component at low energy and a peak near 0.8 eV that may be associated with the transitions near the M point [12]. The spectra suggest that only $\sim 1/3$ of the absorbed photons generate transitions near the Γ and thus β is expected to be modified significantly from the universal value predicted for an idealized chiral Weyl system.

Our room temperature measurements of linear conductivity have been confirmed by a recent study of the temperature, T , dependence performed on samples from the same growth as used in our experiments [44]. Based on the T dependence at low photon energies, it was possible to resolve the intraband (Drude) and interband contributions and determine that $\sigma_1(\omega)$ is dominated by the interband contribution above a photon energy of ~ 0.3 eV. From this we conclude that the cutoff at 0.65 eV is not related to a crossover from intraband to interband absorption. In addition, it was confirmed that $\sigma_1(\omega, T)$ increases throughout the spectral range where we observe the rapid decrease of the CPGE amplitude. Overall, we believe that the linear conductivity data support the hypothesis that the CPGE spectral cutoff can be understood as the onset of transitions whose contribution to the total photocurrent is opposite in sign.

Finally, we believe that regardless of the underlying mechanism, our observation of CPGE photocurrents in a chiral semimetal will stimulate new research directions into the interaction of topological systems with light. For example, the CPGE photocurrent generated by light at normal incidence flows directly into the bulk of crystal, but decays exponentially with increasing depth. This is an unusual example of a longitudinal current created by a transverse light field. Conservation laws suggest that this CPGE will cause charge and pseudospin to accumulate, which would then couple to longitudinal excitations of the medium such as plasmons and phonons. Thus it may be possible to control the amplitude and phase of these collective modes through the polarization state of incident photons, which would be especially

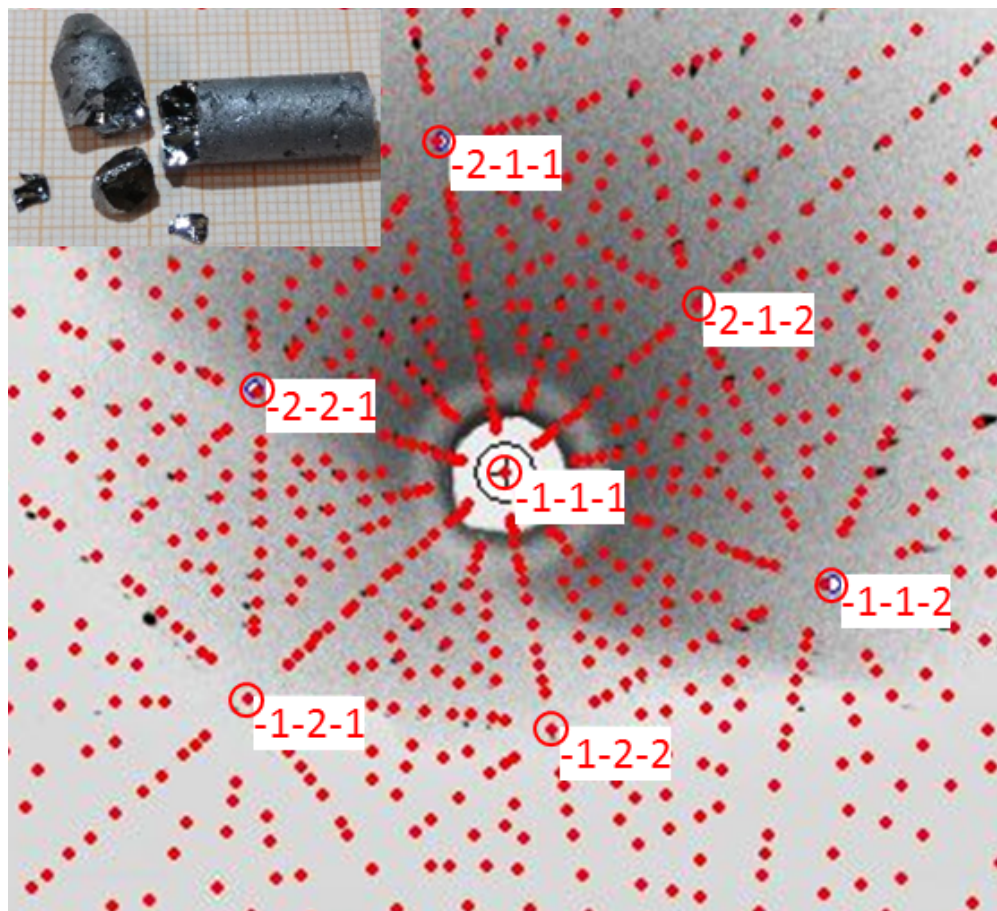


Figure 3.8: **Crystal growth and diffraction** Laue diffraction pattern of a (111) oriented RhSi single crystal superposed with a theoretically simulated pattern. Inset shows picture of the grown RhSi single crystal.

exciting when applied to chiral metals that become superconductors at low temperature.

3.5 Calibrating the CPGE Spectrum

Crystal Growth and Structure Refinement

Single crystals of RhSi were grown from a melt using the vertical Bridgman crystal growth technique. Here the crystal growth was performed with an off-stoichiometric composition with slightly excess Si. First, a polycrystalline ingot was prepared using the arc melt technique with the stoichiometric mixture of Rh and Si metal pieces of 99.99 % purity. Then the crushed powder was filled in a custom-designed sharp-edged alumina tube and finally

sealed inside a tantalum tube with argon atmosphere. The temperature profile for the crystal growth was controlled with a thermocouple attached at the bottom of the tantalum ampoule containing the sample. The sample was heated to 1500°C and then slowly cooled to cold zone with a rate of 0.8 mm/h. Single crystals with average dimension of ~ 15 mm length and ~ 6 mm diameter were obtained. A picture of the grown crystal is shown in the inset of Fig. 3.8. The crystals were analyzed with a white beam backscattering Laue X-ray diffraction technique at room temperature. The samples show very sharp spots that can be indexed by a single pattern, revealing excellent quality of the grown crystals without any twinning or domains. A Laue diffraction pattern of the oriented RhSi single crystal superposed with a theoretically simulated pattern is presented in Fig. 3.8. The structural parameters were determined using a Rigaku AFC7 four-circle diffractometer with a Saturn 724+ CCD-detector applying graphite-monochromatized Mo-K α radiation. The crystal structure was refined to be cubic P2₁3 (#198) with lattice parameter, $a=4.6858(9)$ Å.

Material Properties

Linear optical properties

We used the reflectivity measurements in the range .08eV - 3eV (Fig. 3.7(a)) and performed Kramers-Kronig analysis to compute the complex index of refraction $\tilde{n} = n + i\kappa$. This and the complex dielectric permittivity $\tilde{\epsilon} = \tilde{n}^2$ are plotted in Fig. 3.9. We additionally calculate $\sigma_1 = 2n\kappa\epsilon_0\omega$ (Fig. 3.7(b)) along with α , t_s , t_p and θ_{in} (Fig. 3.11(a-b)) which are the absorption coefficient, Fresnel transmission coefficients for *s*- and *p*-polarization, and the angle of refraction for 45° angle of incidence. These are defined by

$$\begin{aligned}\theta_{in} &= \arcsin \frac{\sin \theta_i}{n} \\ \alpha &= \frac{2\omega\kappa}{c} \\ t_s &= \frac{2 \cos \theta_i}{\cos \theta_i + \tilde{n} \cos \theta_{in}} \\ t_p &= \frac{2 \cos \theta_i}{\tilde{n} \cos \theta_i + \cos \theta_{in}}\end{aligned}\tag{3.12}$$

where $\theta_i = 45^\circ$ is the angle of incidence of the pump light.

We compare the predicted optical conductivity of the Γ and R nodes in RhSi with our measured σ_1 in Fig. 3.7(b) and Fig. 3.10(a). The fraction of the total optical conductivity that represents the predicted linear conductivity is shown in Fig. 3.10(b).

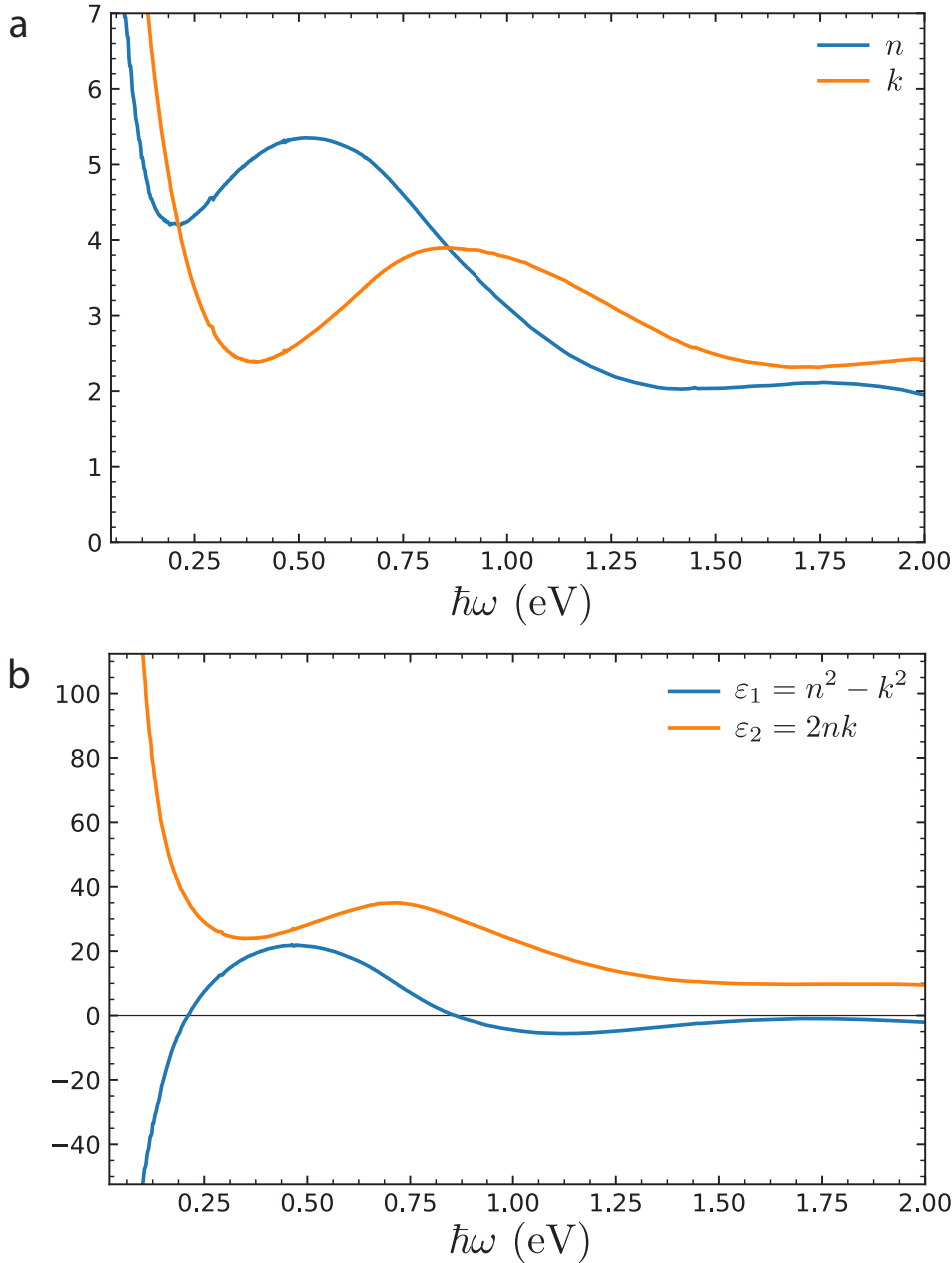


Figure 3.9: **Refractive index** (a) The real and imaginary parts of the refractive index. (b) The real and imaginary parts of the complex dielectric function.

Scattering time (τ)

Using the measured value of σ_{dc} , the equilibrium scattering time can be inferred to be $\tau = 8.6$ fs from $\sigma_1(\omega)$ using the form for the Drude conductivity

$$\sigma_1(\omega) = \frac{\sigma_{dc}}{1 + \omega^2\tau^2}. \quad (3.13)$$

Terahertz index of refraction

The complex index of refraction at THz frequencies determines the impedance mismatch between RhSi and free space. We can obtain an accurate estimate of \tilde{n} in this frequency range from the dc conductivity. Given the value of τ determined in the previous section, the THz emission lies in the low frequency limit of the optical conductivity, where $\omega\tau \ll 1$ and $\sigma(\omega) \rightarrow \sigma_{dc}$. In this regime, the complex permittivity at low frequency is

$$\tilde{\epsilon}(\omega) = -\frac{\tilde{\sigma}(\omega)}{i\omega} = \frac{i\sigma_{dc}}{\omega}. \quad (3.14)$$

The complex index of refraction is then given as,

$$\tilde{n} \equiv n + i\kappa = \sqrt{\frac{\tilde{\epsilon}(\omega)}{\epsilon_0}} = (1 + i)\sqrt{\frac{\sigma_{dc}}{2\epsilon_0\omega}} \quad (3.15)$$

which at 1 THz is equal to $57(1 + i)$. Although the Kramers-Kronig analysis may be somewhat unreliable for photon energies less than ~ 10 meV, it agrees with our analysis and gives $\tilde{n}(1\text{THz}) = 51 + 57i$, confirming that Eq. 3.15 is correct. When calculating $\beta\tau$ in our analysis, we use $\tilde{n}(\omega)$ to find the frequency dependent transmission of the THz radiation from RhSi into free space.

Inferring laser pulse length from emitted THz radiation

It is not feasible using conventional methods such as autocorrelation to characterize the pulse length T of the laser over the entire wavelength range. Lacking a more precise method, we use the THz time traces to estimate the pulse length at each wavelength, since the laser does not necessarily produce the same pulse width across its available wavelength range. We know that the photocurrent scattering time τ is much shorter than the pulse length, which means that the instantaneous current follows the applied electric field squared. The effect of the OAP collection filters, described in a later section, which modify the spectrum of the terahertz radiation is to apply a second derivative to the pulse waveform, since for low frequencies the transmission function's leading term is ω^2 . By making this approximation we find that the full width half maximum of the terahertz pulse t_1 is related to T by the equation

$$t_1 = \sqrt{\frac{1 - 2W(\sqrt{e}/4)}{2}}T \quad (3.16)$$

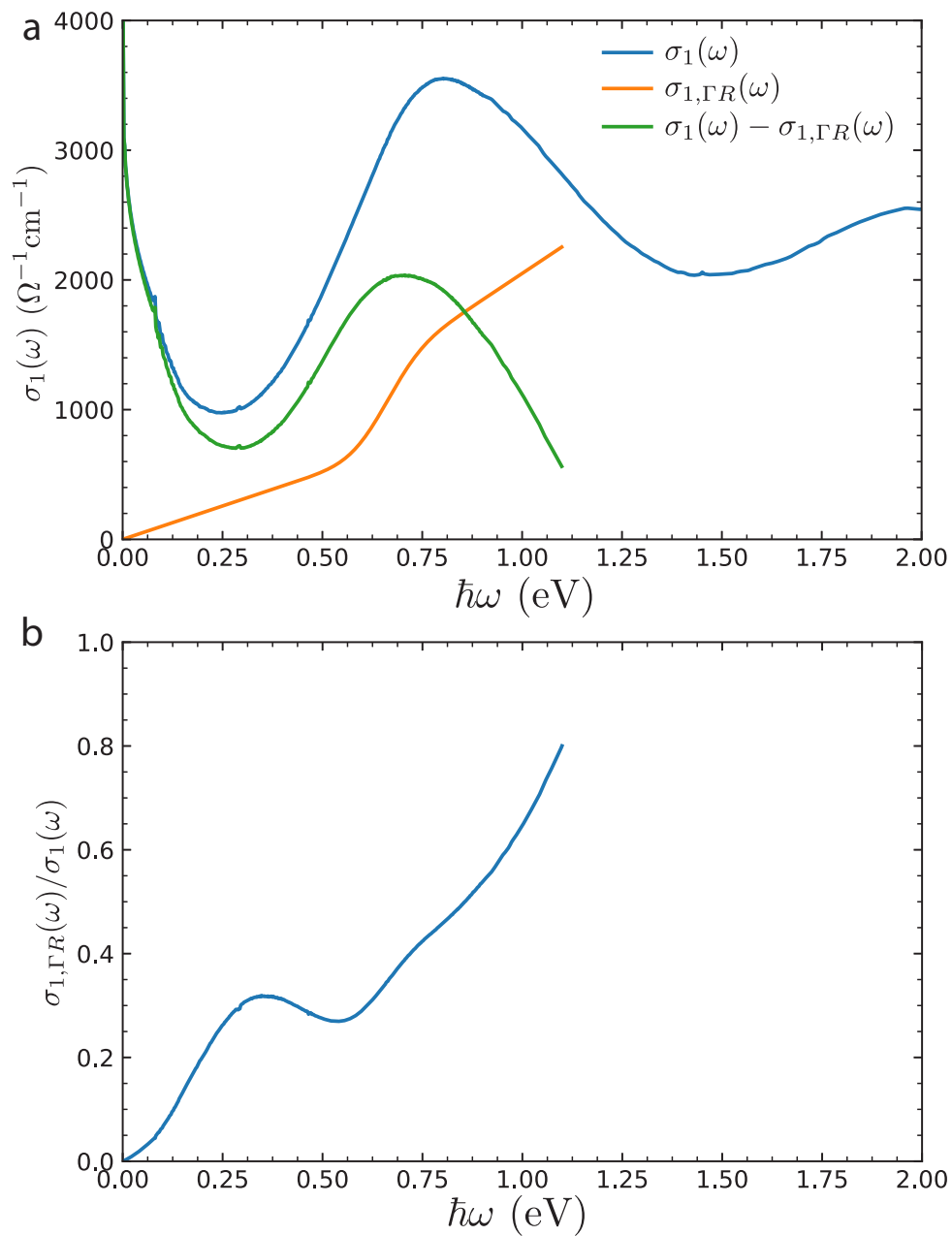


Figure 3.10: **Ideal conductivity** (a) Here we compare the ideal Γ and R band conductivity, $\sigma_{1,\Gamma R}$, with the total conductivity of RhSi, σ_1 . (b) The fraction of σ_1 which constitutes the ideal Weyl conductivity.

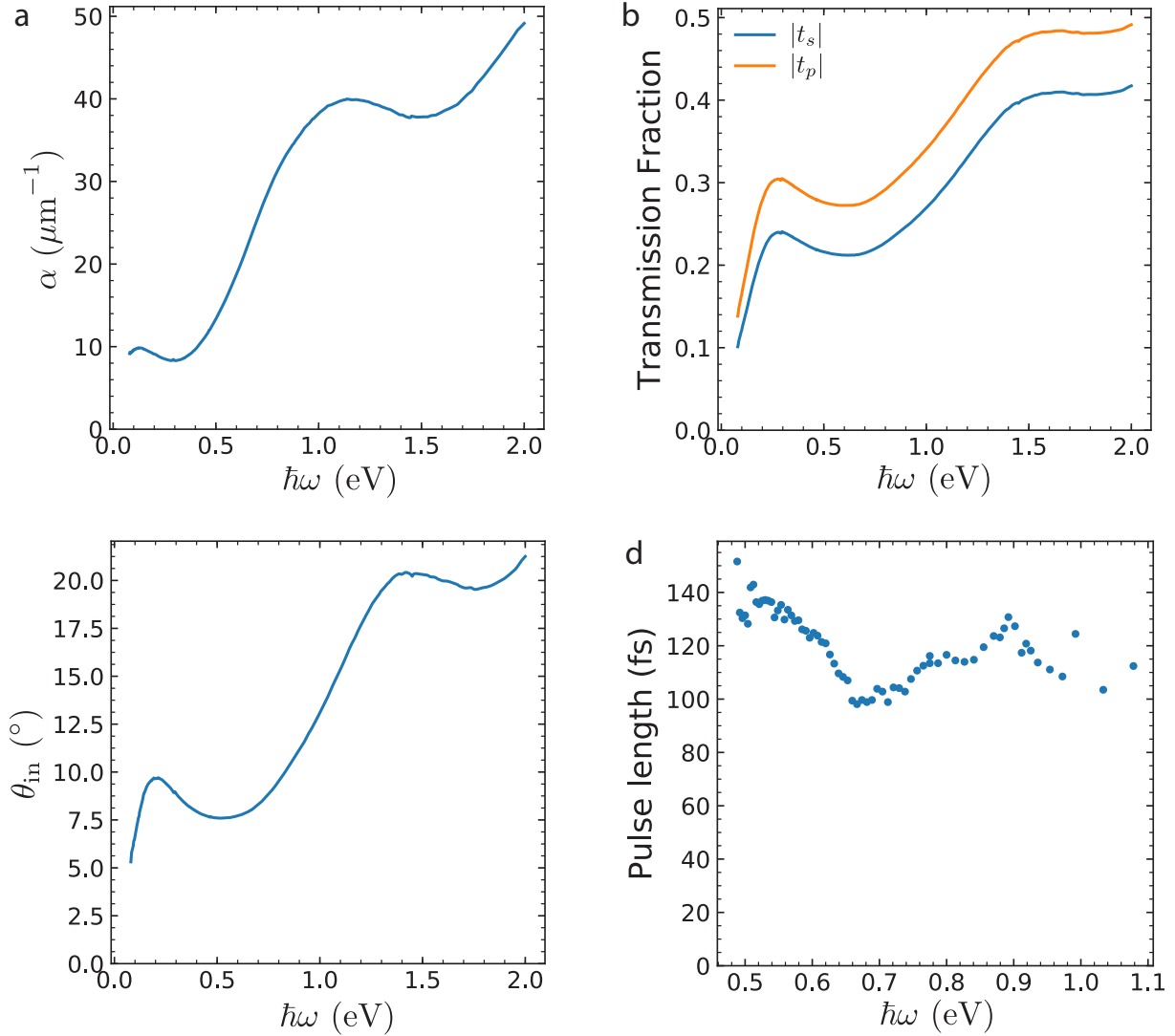


Figure 3.11: **Material properties** (a) Power absorption coefficient α . (b) Fresnel transmission coefficient magnitudes $|t_s|$ and $|t_p|$. (c) Angle of refraction for incident angle $\theta_i = 45^\circ$. (d) Pump pulse length T estimated from the emitted terahertz waveforms.

where $W(z)$ is the Lambert W function, or product log. This allows us to calculate an approximate pulse length for each wavelength. The results are presented in Fig. 3.11(d).

Inferring the CPGE amplitude from the detected electro-optic signal

In this section we describe the normalization factors needed to convert from signal at the electro-optic detector to the CPGE saturation coefficient $\beta\tau$. This process involves the following three steps.

1. Determine the time-dependent electric field in the sample that arises from a photo-generated surface current which depends on laser parameters (intensity at the sample) and material parameters (β , τ , Fresnel coefficients, etc.).
2. Compute the Fourier transform of the terahertz pulse, then apply two filters to it. The first is the frequency-dependent transmission of the radiation into free space, $1/(\tilde{n}(\omega) + 1)$. The second is the transfer function of the collection optics, $\mathcal{F}(\omega)$, that quantifies the fraction of radiation that is collected by the system and transferred to the ZnTe detection crystal.
3. Compute the inverse Fourier transform of the resulting spectrum, then convert the resulting time-dependent electric field at the ZnTe surface crystal to signal at the output of the biased photodetector scheme.

In order to obtain the value of $\beta\tau$ of RhSi, we assume $\beta = \beta_0 = \pi e^3/3h^2$ and $\tau = 1$ fs for all pump frequencies in this calculation. Then, by dividing the amplitude of the measured signal to the expected signal given all experimental parameters, we yield a value for $\beta\tau$ at each pump frequency in units of ($\beta_0 \times \text{fs}$).

1. Calculation of the radiated field from the sample

Assume we have some CPGE coefficient β . For circularly polarized light, CPGE is given by

$$\frac{dj}{dt} = \beta|E|^2. \quad (3.17)$$

As laser light travels through a material at angle θ_{in} relative to the normal direction z , its intensity decays according to the (power) attenuation coefficient along the direction of propagation, $r_k = z/\cos\theta_{in}$:

$$|E|^2 = E_0^2 e_k^{-\alpha r_k}. \quad (3.18)$$

The sheet current density generation rate is then given by

$$\begin{aligned} \frac{dK}{dt} &= \int_0^\infty dz \frac{dj}{dt} \sin\theta_{in} \\ &= \beta E_0^2 \sin\theta_{in} \int_0^\infty dz e_k^{-\alpha z/\cos\theta_{in}} \\ &= \beta \frac{1}{2\alpha} E_0^2 \sin 2\theta_{in} \end{aligned} \quad (3.19)$$

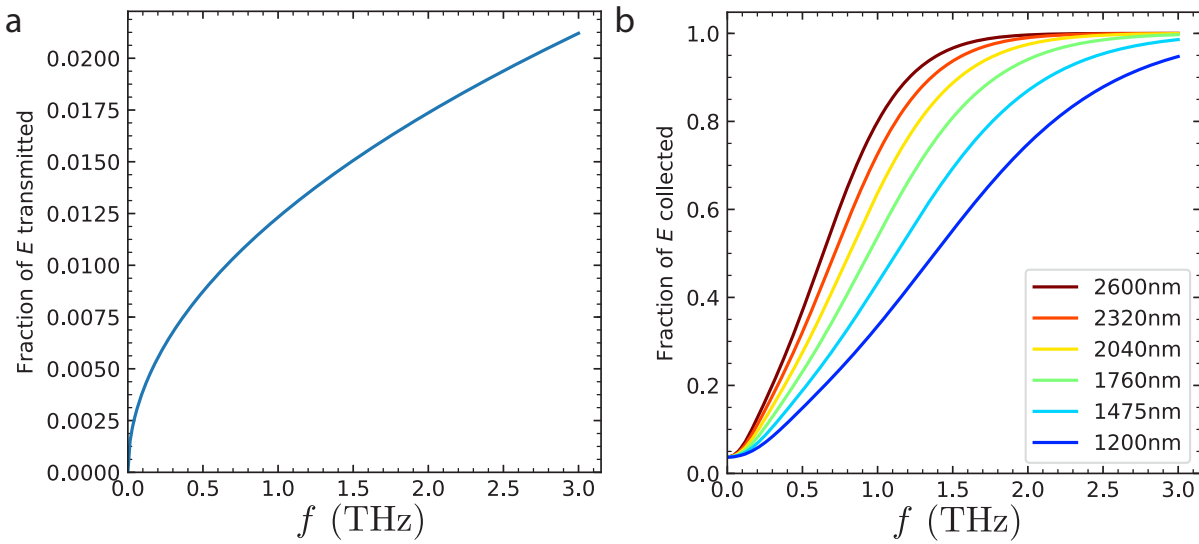


Figure 3.12: **Surface THz transmission and collection filter** (a) Fraction of terahertz radiation transmitted from bulk into free space, determined by dc conductivity and optical conductivity measurements. (b) Fraction of terahertz collected and collimated by the OAP.

and the saturation current density is

$$K = \beta\tau \frac{1}{2\alpha} E_0^2 \sin 2\theta_{in}. \quad (3.20)$$

The factor of $\sin \theta_{in}$ represents the fraction of the current parallel to the surface, which is what radiates into free space. Since the scattering rate τ is much less than the pulse length T , the current amplitude follows the electric field squared amplitude and will radiate in the THz regime. The radiated electric field amplitude can be found as follows. From Ampère's law we have

$$\begin{aligned} E_{\tilde{n}} \frac{\tilde{n}}{c} &= B = \frac{\mu_0}{2} K \\ \implies E &= \frac{\mu_0 c}{2\tilde{n}} K. \end{aligned} \quad (3.21)$$

Using the Fresnel transmission coefficient $t = 2\tilde{n}/(\tilde{n} + 1)$, the external radiation is given by

$$E_{ext} = \frac{\mu_0 c}{2\tilde{n}} K t = \frac{Z_0}{\tilde{n} + 1} K. \quad (3.22)$$

Using Eq. 3.20 we get

$$E_{ext}^{THz} = \frac{\beta Z_0 \tau}{2\alpha(\tilde{n} + 1)} E_0^2 \sin 2\theta_{in}. \quad (3.23)$$

The frequency dependence of the factor $1/(\tilde{n}(\omega) + 1)$ is shown in Fig. 3.12(a). Now we must express E_0 in terms of the measured laser parameters average power P , repetition rate f ,

spot size r_0 and pulse duration T . At normal incidence the intensity of the electric field of the pump laser at the surface of the sample is given by

$$I(r, t) = \frac{c\epsilon_0}{2} E^2(r, t) = \frac{c\epsilon_0}{2} E_{\text{ext}}^2 e^{-r^2/r_0^2} e^{-t^2/T^2} \quad (3.24)$$

Integrating over space and time yields the relation

$$E_{\text{ext}}^2 = \frac{2PZ_0}{\pi\sqrt{\pi}fTr_0^2}, \quad (3.25)$$

where we include a factor of $1/2$ to account for 45° angle of incidence. This leaves us with a peak THz electric field of

$$E_{\text{ext}}^{\text{THZ}} = \frac{Z_0^2 \beta \tau t_s t_p P \sin 2\theta_{in}}{\pi\sqrt{\pi}\alpha f T r_0^2 (\tilde{n} + 1)} \quad (3.26)$$

which radiates into free space and eventually is detected through electro-optic sampling. In order to experimentally determine the spectrum of $\beta\tau$, each of the terms in the above equation must be determined as a function of the pump frequency. As discussed earlier, we calculate t_s , t_p , $\theta_{in} = \arcsin 1/(\sqrt{2}n)$ and $\alpha = 2\kappa\omega/c$ as a function of pump frequency based on spectrally resolved reflectivity measurements and Kramers-Kronig analysis which produces the complex index of refraction. These values are plotted in Fig. 3.11(a-c). The laser power P is directly measured across the laser's spectral range. We use a concave focal length $F = 50$ cm mirror to focus light on the sample, gives a focused spot size of $r_0 = \frac{2F\lambda}{\pi d}$ where d is the collimated beam diameter.

2. Radiation from the photoexcited region

The THz radiation emitted by the sample is collected by a 45° OAP which collimates the beam. A second OAP then focuses it onto a ZnTe electro-optic sampling (EOS) crystal. In order to calculate the fraction of radiated light collected by the OAP, we start with the formula for the vector potential at location \mathbf{r} from a current density described by $\mathbf{j}(\mathbf{r}, t)$,

$$\mathbf{A}(\mathbf{r}, t) = \frac{\mu_0}{4\pi} \int d^3\mathbf{r}' \frac{\mathbf{j}(\mathbf{r}', t_r)}{|\mathbf{r} - \mathbf{r}'|} \quad (3.27)$$

where t_r is the retarded time. If we assume radiation at a specific frequency ω , the current density in our experiment is given by

$$\mathbf{j}(\mathbf{r}, t) = J_0 \hat{x} \delta(z) e^{-x^2/2r_0^2} e^{-y^2/r_0^2} e^{-(t-x' \sin \theta_i/c)^2/T^2} \quad (3.28)$$

where the term $x' \sin \theta_i/c$ in the final exponential represents the phase delay across the photoexcited spot due to off-normal incidence at angle $\theta_i = 45^\circ$ (Fig. 3.13(a)). The coordinates used in the calculation are shown in Fig. 3.13(b).

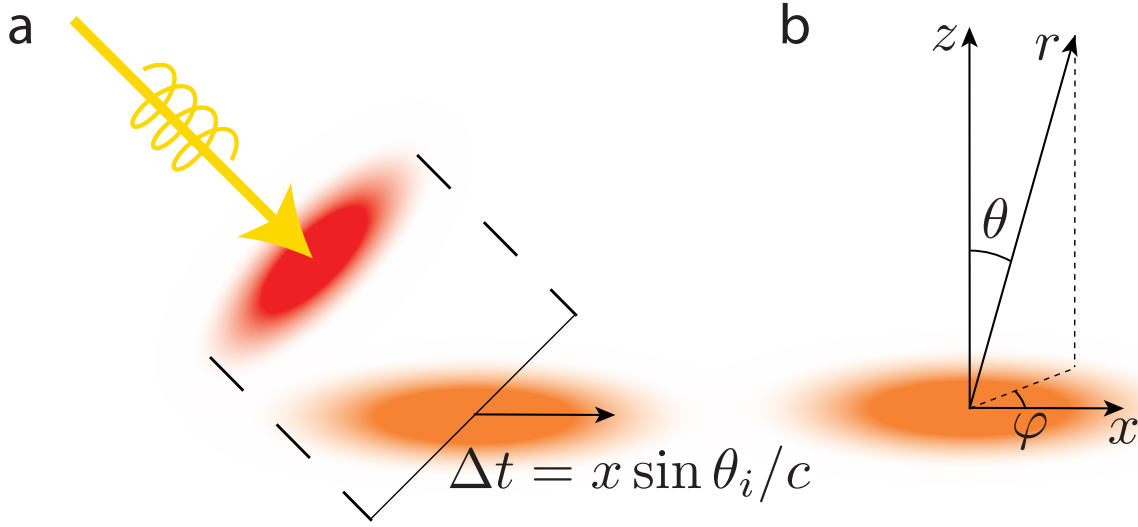


Figure 3.13: **Filter calculation geometry** (a) Illustration of photoexcited current at off-normal incidence. The pump light (red shading) is cast onto the sample which excites a current (orange shading). There is a time delay across the photoexcited region which affects the radiated angle, as in a phased array antenna. (b) Illustration of the polar coordinate system used in the filter calculation.

The retarded time at \mathbf{r} is given by

$$\begin{aligned}
 t_r &= t - |\mathbf{r} - \mathbf{r}'|/c \\
 &= t - \frac{1}{c} \sqrt{r^2 - 2\mathbf{r} \cdot \mathbf{r}' + r'^2} \\
 &\approx t - \frac{1}{c} r (1 - \hat{\mathbf{r}} \cdot \mathbf{r}'/r) \\
 &= t - \frac{r}{c} + \frac{\hat{\mathbf{r}} \cdot \mathbf{r}'}{c} \\
 &= t - \frac{r}{c} + \frac{1}{c} (\sin \theta \cos \phi x' + \sin \theta \sin \phi y').
 \end{aligned} \tag{3.29}$$

where the OAP is in the far field limit $r' \ll r$.

The Fourier transform of the vector potential is

$$\mathbf{A}(\mathbf{r}, \omega) = \frac{\mu_0}{4\pi r} j_0 \hat{x} \int dt e^{i\omega t} \int dx' dy' e^{-\frac{x^2}{2r_0^2}} e^{-\frac{y^2}{r_0^2}} e^{-u^2/T^2} \tag{3.30}$$

where $u = t_r - \frac{x' \sin \theta_i}{c} = t - \frac{r}{c} + (\sin \theta \cos \phi - \sin \theta_i) \frac{x'}{c} + \sin \theta \sin \phi \frac{y'}{c}$. This gives

$$\begin{aligned} \mathbf{A}(\mathbf{r}, \omega) &= \frac{\mu_0}{4\pi r} j_0 \hat{x} e^{-\omega^2 T^2/4} e^{i\omega r/c} \int dx' e^{-\frac{x'^2}{2r_0^2}} e^{i\omega x' (\sin \theta \cos \phi - \sin \theta_i)/c} \\ &\quad \times \int dy' e^{-\frac{y'^2}{r_0^2}} e^{i\omega y' \sin \theta \sin \phi/c} \end{aligned} \quad (3.31)$$

$$= \frac{\mu_0}{4\sqrt{2}r} r_0^2 \sqrt{\pi} j_0 \hat{x} e^{-\omega^2 T^2/4} e^{i\omega r/c} e^{-\frac{r_0^2 \omega^2}{2c^2} (\sin \theta_i - \sin \theta \cos \phi)^2} e^{-\frac{r_0^2 \omega^2}{4c^2} \sin^2 \theta \sin^2 \phi} \quad (3.32)$$

The fraction of the total radiation captured by the OAP is given by

$$\mathcal{F}(\omega) = \int_{OAP} d\theta d\phi \sin \theta E(\omega, \theta, \phi) \bigg/ \int_{2\pi} d\theta d\phi \sin \theta E(\omega, \theta, \phi). \quad (3.33)$$

The second integral is integrated over the upper half-sphere ($0 < \theta < \pi/2$) because we only consider the radiation emitted away from the sample, not into it. All θ - and ϕ -independent factors can be removed from the integrand, so we can use the form

$$E(\theta, \phi) \propto \cos \theta e^{-\frac{r_0^2 \omega^2}{2c^2} (\sin \theta_i - \sin \theta \cos \phi)^2} e^{-\frac{r_0^2 \omega^2}{4c^2} \sin^2 \theta \sin^2 \phi} \quad (3.34)$$

in the integrand. The integral depends on spot size, r_0 , which is variable across the spectral range of the pump laser. We calculate this integral numerically for each pump wavelength. $\mathcal{F}(\omega)$ is plotted for several pump wavelengths in Fig. 3.12(b) as a function of $\nu = \omega/2\pi$. For small wavelengths relative to the excitation spot size, the radiation emits at the specular direction relative to the incoming pump light.

3. Electro-optic detection using ZnTe

The last step in the calibration is the conversion of the electric field at the surface of the ZnTe crystal to the signal at the output of the biased photodetector scheme. Detection of the THz field is performed through electro-optic sampling (EOS) in ZnTe (110). In this technique the THz electric field induces transient birefringence, Δn , in the ZnTe, which is detected by a co-propagating probe beam at 800 nm. Our analysis is based on the detailed studies of the EOS in technique presented in Refs. [3, 19]. For THz frequencies below 3 THz we neglect dispersion in ZnTe and assume a real index $n = 2.85$ [47].

The transient birefringence generates a polarization rotation in the probe beam. We measure the rotation using an optical bias scheme [9, 33] that yields a gain factor of 88 as compared with the conventional balanced detector measurement. In the conventional scheme, the fractional change in the balanced output is given by,

$$\frac{\Delta V(\tau)}{V} = \frac{\omega n^3 r_{41}}{2c} \int_0^L dz \int_{-\infty}^{\infty} dt E_{THz}(z, t) I_0(z, t - \tau) \quad (3.35)$$

where ω is the angular frequency of the probe pulse, c is the speed of light, L is the propagation distance through the crystal, E_{THz} is the THz field strength, $r_{41} = 4$ pm/V is the electro-optic coefficient of ZnTe at 800 nm, $n = 2.85$ is the index of refraction of ZnTe and

$$I_0(z, t - \tau) = I_0 \exp\{-[z - v_g(t - \tau)]^2 / (v_g T_{pr})^2\} \quad (3.36)$$

is the normalized intensity of the 800 nm probe beam with pulse duration, T_{pr} , which propagates with group velocity v_g .

THz transients with bandwidth less than 3 THz, Eq. 3.35 simplifies to,

$$\frac{\Delta V(\tau)}{V} = \frac{\omega n^3 r_{41} L}{2c} \int_{-\infty}^{\infty} dt E_{THz}(t) I_0(t - \tau). \quad (3.37)$$

Because the duration of the probe pulse is approximately 35 fs, much less than the time scale of the THz transient, we make the approximation that $I_0(t - \tau) \rightarrow \delta(t - \tau)$ to obtain [9]

$$\frac{\Delta V(\tau)}{V} = \frac{\omega n^3 r_{41} L}{2c} E_{THz}(\tau). \quad (3.38)$$

An additional factor of $2/(n + 1)$ is needed because the THz field is partially reflected at the surface of the ZnTe. Finally, we substitute E_{THz} with the expression in Eq. 3.26 (after applying the frequency dependent collection filters) and as discussed earlier set $\beta\tau = \beta_0 \times 1$ fs. This gives an expected EOS signal for each pump frequency based on laser parameters, material properties and the experimental geometry, and by comparing the measured value with the expected value we obtain $\beta\tau$ in units of ($\beta_0 \times$ fs). The results are previously plotted in Fig. 3.6.

Chapter 4

Surface Photogalvanic Effects

4.1 Surface States

Despite the fundamental nature of the edge state in topological physics, direct measurement of electronic and optical properties of the Fermi arcs of topological semimetals has posed a significant experimental challenge, as their response is often overwhelmed by the metallic bulk. However, laser-driven currents carried by surface and bulk states can propagate in different directions in nonsymmorphic crystals, allowing for the two components to be easily separated. Motivated by a theoretical prediction [13], we have measured the linear and circular photogalvanic effect currents deriving from the Fermi arcs of the nonsymmorphic, chiral Weyl semimetal RhSi over the incident photon energy range 0.45 – 1.1 eV. Our data are in good agreement with the predicted spectral shape of the circular photogalvanic effect as a function of photon energy, although the direction of the surface photocurrent departed from the theoretical expectation over the energy range studied. Surface currents arising from the linear photogalvanic effect were observed as well, with the unexpected result that only two of the six allowed tensor elements were required to describe the measurements, suggesting an approximate emergent mirror symmetry inconsistent with the space group of the crystal.

Protected edge states like the current-carrying edge state of the quantum Hall effect [24, 54] or the spin-momentum locked surface states of bulk topological insulators [18, 27] are a universal property of topological matter. In Weyl semimetals, which host emergent, massless, chiral Weyl fermions, the topological edge state comprises open Fermi surface arcs formed of helicoidally dispersing, spin-momentum locked quasiparticles that are constrained to the sample surface [65, 1]. The arcs connect the projections of opposite chirality Weyl nodes, curving in complementary shapes on the 2D surface Brillouin zones on the opposite sides of the crystal. The existence of these states has been confirmed by ARPES [69, 40, 68, 5] and quasiparticle interference measurements [28] and have been shown to play a central role in quantum oscillations [53, 45]. However, despite a number of predictions focused on the role of the Fermi arcs in topological semimetal physics [32, 59, 61, 46, 23, 66], their transport and optical properties have largely remained hidden, as they are often dominated by bulk

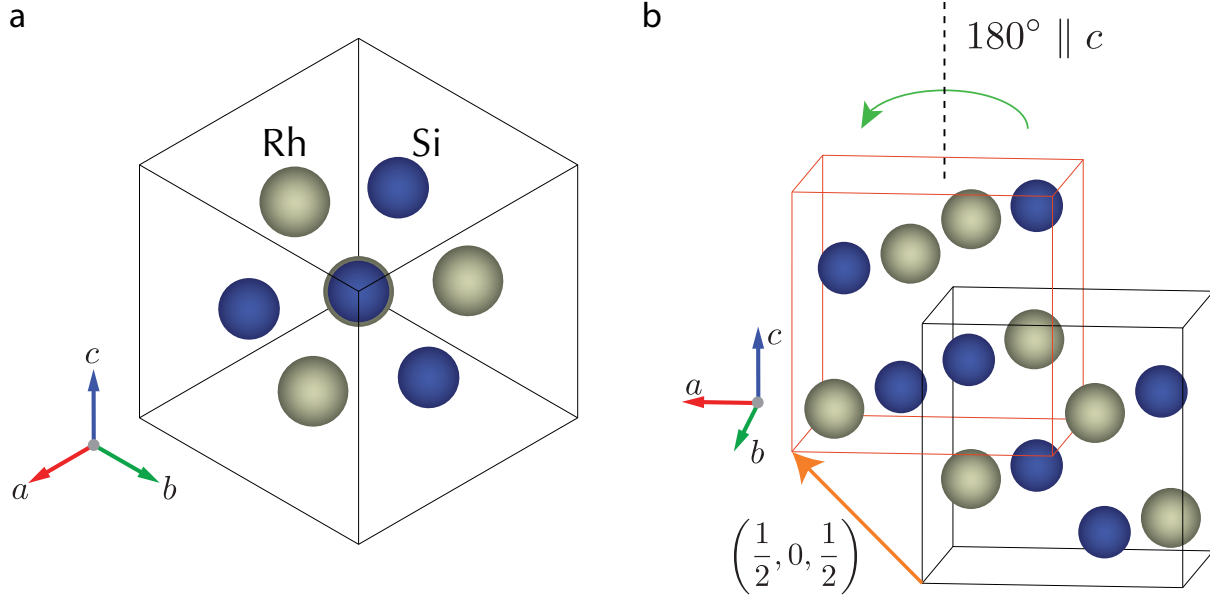


Figure 4.1: **RhSi Crystal Structure** (a) Unit cell displayed with the (111) direction pointing out of the page, showing the three-fold rotational symmetry of the crystal. (b) Extended RhSi structure, showing two alternate unit cells offset by $(\frac{1}{2}, 0, \frac{1}{2})$. When the unit cell marked by the orange frame is rotated 180° about the z axis, it is identical to the unit cell marked by the black frame, illustrating the two-fold screw symmetry.

response functions. For example, experiments aimed at measuring the linear conductivity of surface states run into difficulties because of shorting by the metallic bulk that lies below.

We will demonstrate experimentally that the second-order nonlinear conductivity, which describes the strength and symmetry of the photogalvanic effects (PGEs), provides a means to selectively probe surface state electronic properties in Weyl semimetals. The PGEs are phenomena in which optical excitation generates a dc current that arises from intrinsic breaking of inversion symmetry, rather than applied bias voltage or inhomogeneous doping [42, 50]. A further defining property of PGEs is sensitivity of the direction of photocurrent, \mathbf{J} , to the polarization state of the optical electric field \mathbf{E} , as described by the phenomenological relation,

$$J_i = \gamma_{ijk} E_j E_k + i\beta_{ij} (\mathbf{E} \times \mathbf{E}^*)_j. \quad (4.1)$$

The first term on the right-hand side of Eq. 4.1 describes the LPGE in terms of the polar tensor γ_{ijk} and the second term corresponds to the CPGE in terms of the axial tensor β_{ij} . Both PGE response tensors are zero in the presence of inversion symmetry.

As discussed in the previous chapter, the CPGE has received particular attention in topological semimetals like RhSi because they crystallize in structures in which all mirror symmetries are broken, forming a chiral medium [12, 64, 11, 17, 37, 48, 38, 14, 57, 60, 43,

51, 39, 10, 52, 22, 29]. While the prediction of QCPGE is disrupted by the existence of trivial bands in RhSi, the polarization selection rules for both CPGE and LPGE observed on (111) faithfully follow constraints imposed by the symmetry of the bulk [55]. As we show below, these constraints provide a route to selectively probe the Fermi arc surface states on the (001) surface.

4.2 Symmetry Considerations

The space group of RhSi (#198) contains two operations: a 3-fold rotation about the (111) direction and a nonsymmorphic screw symmetry in which a 2-fold rotation about the z axis is combined with a translation by $(1/2, 0, 1/2)$. Fig. 4.1 illustrates these symmetries in the crystal structure. In describing bulk response functions, where perfect translational symmetry is assumed, the screw operation imposes the same constraints on response tensors as 2-fold rotation. The combination of the 3- and 2-fold rotational symmetry greatly reduces the number of nonvanishing elements of the γ_{ijk} and β_{ij} tensors that describe the bulk PGE response. Only tensor elements $\gamma_{xyz} = \gamma_{yzx} = \gamma_{zxy}$ of the LPGE response are nonzero, and the CPGE tensor is purely diagonal with $\beta_{ij} = \beta\delta_{ij}$. Note that given the reduction of the CPGE tensor to a scalar, Eq. 4.1 predicts that the CPGE current flows parallel to the wavevector of excitation light, independent of the crystal orientation.

As discussed previously, light incident on the (111) surface verified the symmetry-based predictions for the bulk response functions [55]. The CPGE signal was below the noise level at normal incidence, consistent with the prediction that it flows parallel to the optical wavevector and therefore does not radiate in the direction of specular reflection (Fig. 4.2). As further confirmation, THz radiation from CPGE current two orders of magnitude above the noise level was observed when the angle of incidence was set 45° from the normal direction, where the bulk symmetry and measurement geometry imply a radiating CPGE current parallel to the surface.

The experiments described below were stimulated by the prediction that the photogalvanic response to light normally incident on the (001) surface would be qualitatively different than (111), directly revealing the presence of topologically protected surface states through the observation of a surface current [13]. As discussed more in depth in a later section, for the (001) face, the symmetry of the bulk predicts that LPGE as well as CPGE current flows normal to the surface, in which case no radiation from PGEs is expected, as with CPGE on the (111) surface. The crucial ingredient leading to the prediction of PGE currents parallel to the (001) is the presence of a screw symmetry in the space group. Truncation of the crystal at (001) disrupts the translational component of the screw operation and violates the effective 2-fold symmetry. Consequently there is no operation, other than the identity, that transforms the (001) surface to itself and all tensor elements disallowed by bulk symmetry become allowed for surface-localized electronic states. In particular the six elements with only x and y indices (i.e., γ_{xxx} , γ_{xxy} , γ_{xyy} , γ_{yxx} , γ_{yyx} and γ_{yyy}) are not forbidden, allowing for in-plane photocurrent and specular THz radiation to be generated by light at normal

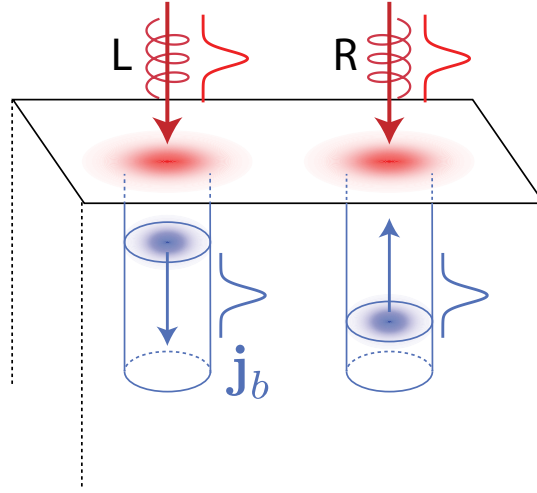


Figure 4.2: **Bulk CPGE Symmetry** When circularly polarized light is incident on RhSi, the bulk CPGE current will be directed perpendicular to the surface, with its sign determined by the incident light's handedness. L and R refer to left- and right-handed circular polarization and \mathbf{j}_b refers to the bulk CPGE current.

incidence.

4.3 Experimental Results

The apparatus used to observe short-lived surface-currents via their THz radiation is shown in Fig. 4.3(a), and is similar to that used to probe bulk photocurrents in the previous chapter, shown with additional details in Fig. 3.3. The excitation source was an optical parametric amplifier pumped by an amplified Ti:Sapphire laser, producing wavelength tunable pulses from 1150-2600 nm (0.48-1.1 eV) and pulse duration ≈ 100 fs. In-plane photogalvanic currents radiate THz pulses into free space that are focused onto a ZnTe crystal for time-resolved electro-optic sampling of the THz transient (whereas the radiation due to through-plane bulk photocurrents does not emerge from the sample) [55].

Figs. 4.3(b) and 4.3(c) show the experimental configurations used to measure the direction of the PGE currents for different polarization states of the normally incident radiation. The incident light was chosen to be either left or right circularly polarized, or linearly polarized with the plane of polarization rotatable through an angle θ (Fig. 4.3(b)). In addition, the sample was also rotated about the optical axis by an angle ϕ (Fig. 4.3(c)). The crystal axes were determined by Laue diffraction (Fig. 4.4) and the sample rotation stage was ini-

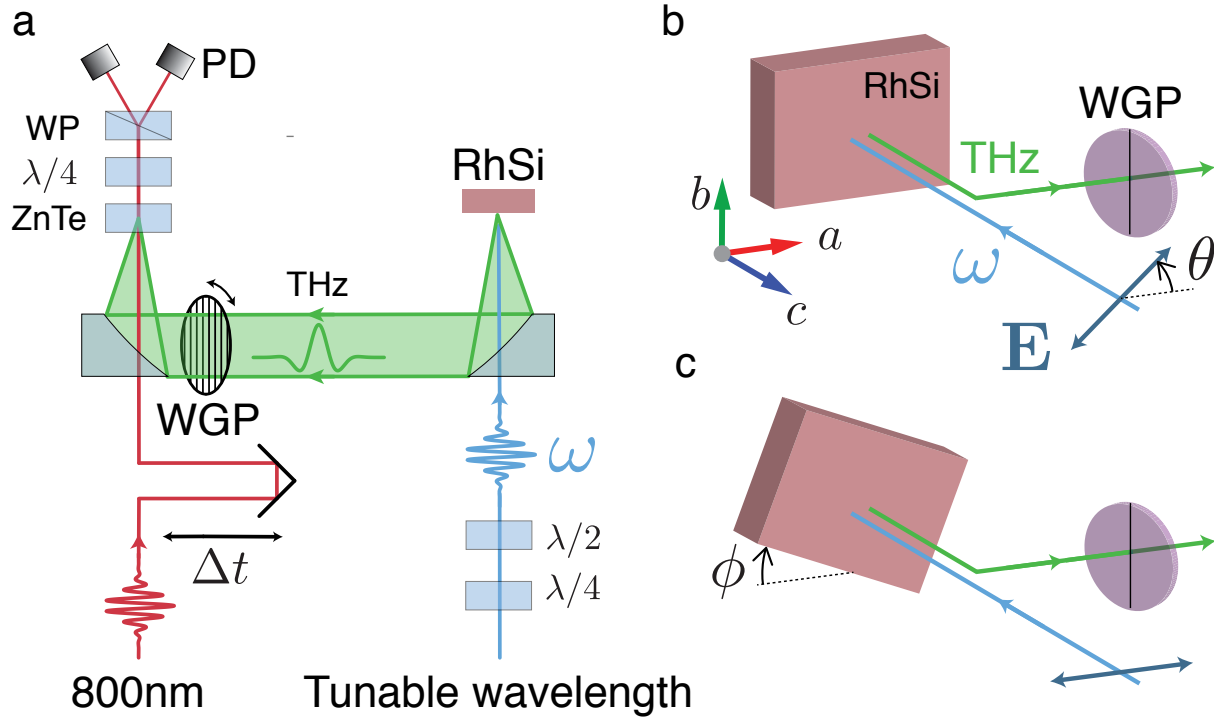


Figure 4.3: **Experimental Diagram for surface currents** (a) Schematic of experiment used to detect photogalvanic currents in RhSi via terahertz detection. Near infrared (NIR) light with tunable wavelength and polarization is focused onto the (001) RhSi surface at normal incidence. Terahertz radiation is collected and collimated using off-axis parabolic mirrors. It passes through a wire-grid polarizer before being focused onto a ZnTe crystal. Light with $\lambda = 800$ nm and variable time delay Δt copropagates through the ZnTe for electro-optical detection of the terahertz. PD, photodiode; WP, Wollaston prism; WGP wire grid polarizer; $\lambda/2$, half-wave plate; $\lambda/4$, quarter-wave plate. (b) In one experimental configuration, the sample is kept fixed while the pump polarization is rotated by angle θ . The sample axes are set such that [100] and [010] are horizontal and vertical in the lab frame respectively. (c) In the second configuration, the pump polarization is fixed at $\theta = 0$ and the sample is rotated by and angle ϕ .

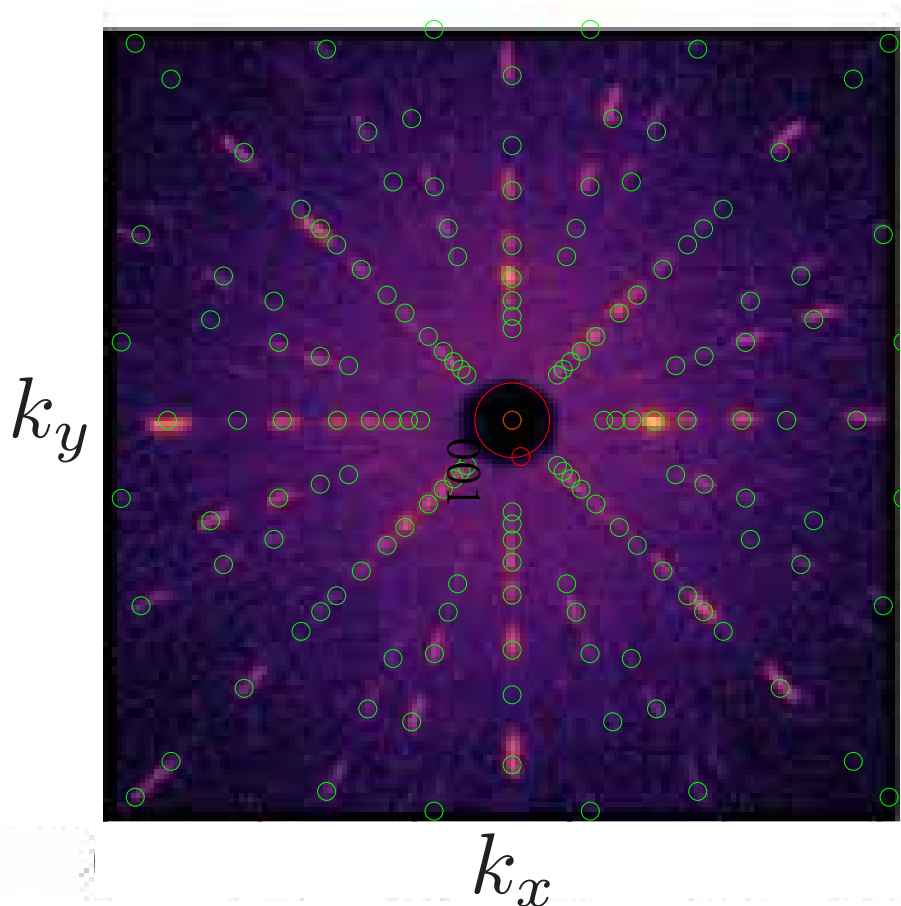


Figure 4.4: **Laue Diffraction Pattern** Laue diffraction measurement overlaid with the predicted diffraction peaks of the 001 surface of space group 198.

tialized such that at $\phi = 0$ (100) and (010) crystal axes are horizontal and vertical in the laboratory reference frame, respectively. Samples from two different batches were used in the experiments. A Flack parameter of $-0.06(4)$ was measured for both samples, indicating a very high enantiomeric purity [16]. Further details of the crystal characterization is given in Table 4.1.

Figure 4.5(a) shows direct evidence for the generation of in-plane helicity-dependent photocurrent at normal incidence on the (001) surface. The THz amplitude plotted on the vertical axis is the difference in radiation generated by left and right circularly polarized light $\hbar\omega = 0.8$ eV and is thus a measure of the CPGE. The two plots show the dependence of the horizontal (H) and vertical (V) components of the CPGE amplitude on the angle of rotation, ϕ , of the sample about the optic axis. The fact that CPGE is observable at normal incidence already suggests that in-plane photocurrent is generated. As Fig. 4.5(b)

Table 4.1: Room temperature single crystal Refinement result for RhSi.

Formula	RhSi
F.W. (g/mol);	131
Space group; Z	P213 (No. 198); 4
a (Å)	4.6858(9)
V (Å ³)	102.88(6)
Absorption Correction	Multi-scan
Extinction Coefficient	0.22(1)
θ range (°)	6.1-51.3
No. reflections; Rint	5013; 0.0341
No. independent reflections	392
No. parameters	9
R1; wR2 (all I)	0.0132; 0.0341
Goodness of fit	2.410
Diffraction peak and hole (e-/Å ³)	0.760; -1.147

illustrates, the dipole radiation pattern for normally directed photocurrent has a node at the angle of specular reflection from the surface and therefore does not directly generate THz radiation, although weaker radiation from multiple scattering is possible. The proof that the observed radiation does indeed arise from an in-plane CPGE current is the dependence of the H and V components of the CPGE radiation on ϕ . The solid lines in Fig. 4.5(a) are fits to $A \cos(\phi - \phi_0)$ and $A \sin(\phi - \phi_0)$, with $\phi_0 \approx 10^\circ$ for both components. This dependence of the CPGE amplitude on ϕ proves that as the sample rotates the CPGE current rotates as well, maintaining an angle ϕ_0 with respect to the (001) direction. This behavior is contrast to a normally directed CPGE current, which would be independent of ϕ .

Having shown that a CPGE surface current is observed in violation of the restrictions placed by the symmetry of the bulk, we next tested the theoretical prediction for the dependence of CPGE amplitude and direction on $\hbar\omega$. The surface bands responsible for Fermi arcs in RhSi comprise two intertwined helicoids with opposite spin polarization, as illustrated schematically in Fig. 4.6 in a plot of energy vs. in-plane momentum [15, 57]. The helicity-dependent in-plane CPGE current arises from spin-flip optical transitions between the two helicoids, as indicated by the arrows in Fig. 4.6.

The comparison of theoretical and experimental measured spectra shown in Figs. 4.7(a) and 4.7(b) strongly implicates transitions involving Fermi arc states as the origin of the CPGE effect at the (001) surface. Fig. 4.7(a) compares the observed CPGE amplitude (closed circles) as a function of ω with the spectra predicted using Wannier functions derived from first principles calculations (solid lines) [13]. The two curves in Fig. 4.7(a) correspond to the H and V components of the CPGE current, proportional to β_{xz} and β_{yz} , respectively. The

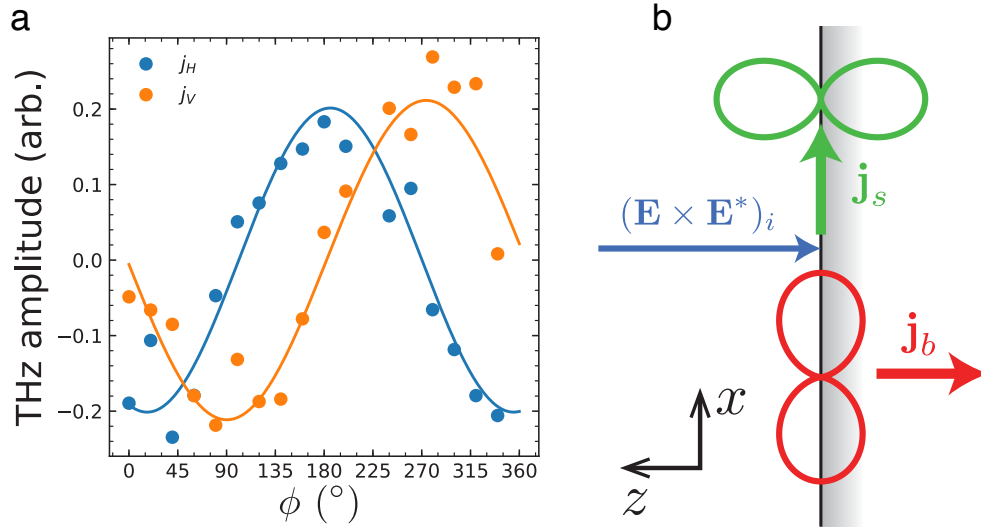


Figure 4.5: **CPGE on (001)** (a) Amplitude of CPGE for horizontally and vertically polarized THz emission as a function of sample orientation ϕ . (b) Schematic showing directions of bulk PGE (\mathbf{j}_b , red) and surface PGE (\mathbf{j}_s , green) with normally incident light on the 001 surface of RhSi with the resulting radiation patterns. In general \mathbf{j}_s has components in x and y .

spectra were uniformly consistent between multiple points on the surfaces of the two samples studied. Fig. 4.7(b) shows that the evident discrepancy between theoretical prediction and experiment is resolved to a remarkable extent when the energy axis is scaled by a factor of 1.25. Such an increase in the energy of optical transitions can be found when screening effects beyond the local density approximation are considered¹.

To fully characterize the nonlinear response, we measured the response to linear polarization, i.e., LPGE, in addition to the CPGE. Although Ref. [13] did not provide theoretical predictions for the LPGE, the implication of that work is that since 2-fold rotational symmetry is broken at the surface, the six elements of γ_{ijk} that contain only x and y indices, forbidden in the bulk response, become allowed at the (001) surface. This symmetry-based argument would then predict the existence of in-plane LPGE currents whose directions need not correlate or align with the cubic axes of the crystal.

As was the case with circularly polarized light, THz radiation was readily observed at normal incidence under photoexcitation with linearly polarized light. To determine the com-

¹Rescaling of the energy by a factor 1.25 can be obtained when DFT/LDA theory is augmented by inclusion of a certain amount of Hartree-Fock exchange using hybrid density functionals, for example in the Heyd, Scuseria, and Ernzerhof (HSE) approach. G. Chang and M. Z. Hasan, private communication (2021).

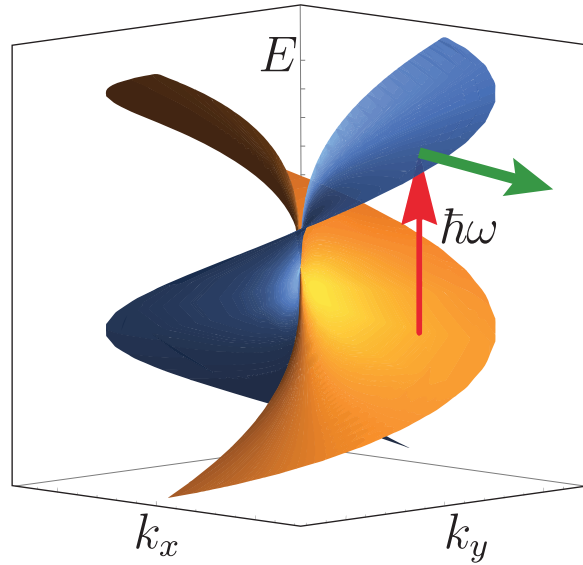


Figure 4.6: **Helicoid Surface Bands** Schematic of surface helicoid bands including a photoexcitation of an electron at energy $\hbar\omega$ (red arrow) and the induced current (green arrow).

ponents of the LPGE tensor we resolved the THz amplitude into the H and V channels, varying the polarization angle of the pump beam while keeping the sample fixed. Fig. 4.8(a) shows the amplitude of the H and V components as a function of the angle of linear polarization, θ . The solid lines are fits to $A \cos(2\theta - \theta_0) + B$. The six independently determined parameters, i.e., the amplitude of the cosine component, A , offset angle θ_0 , and offset amplitude B for the H and V channels, are sufficient to determine the relative amplitude of all six elements of γ_{ijk} that contribute to an in-plane current at normal incidence. This can be seen as follows.

Both THz polarizations were acquired at each pump wavelength before the wavelength was changed. This required that the ZnTe crystal and THz polarizer be adjusted to select for either horizontal or vertical emitted THz polarization. In the optical biasing scheme used here [9, 33], this resulted in a small difference in the measured THz amplitude as the probe and THz beams passed through slightly different positions on the ZnTe detection crystal each time it was rotated. Through repeated measurements, we estimate that this error was, on average, $\sim \pm 7.5\%$ of the total THz amplitude. We have accounted for this error with error bars on the plots of the LPGE parameters.

For a given pump wavelength, we rotate the polarization while the sample remains fixed, and the electric field is given by $\mathbf{E}(\theta) = E_0(\cos \theta, \sin \theta)$. This gives photogalvanic currents

$$\begin{aligned} J_x &= (\gamma_{xxx} \cos^2 \theta + \gamma_{xyy} \sin^2 \theta + 2\gamma_{xxy} \cos \theta \sin \theta) E_0^2 \\ J_y &= (\gamma_{yxx} \cos^2 \theta + \gamma_{yyy} \sin^2 \theta + 2\gamma_{yyx} \cos \theta \sin \theta) E_0^2. \end{aligned} \quad (4.2)$$

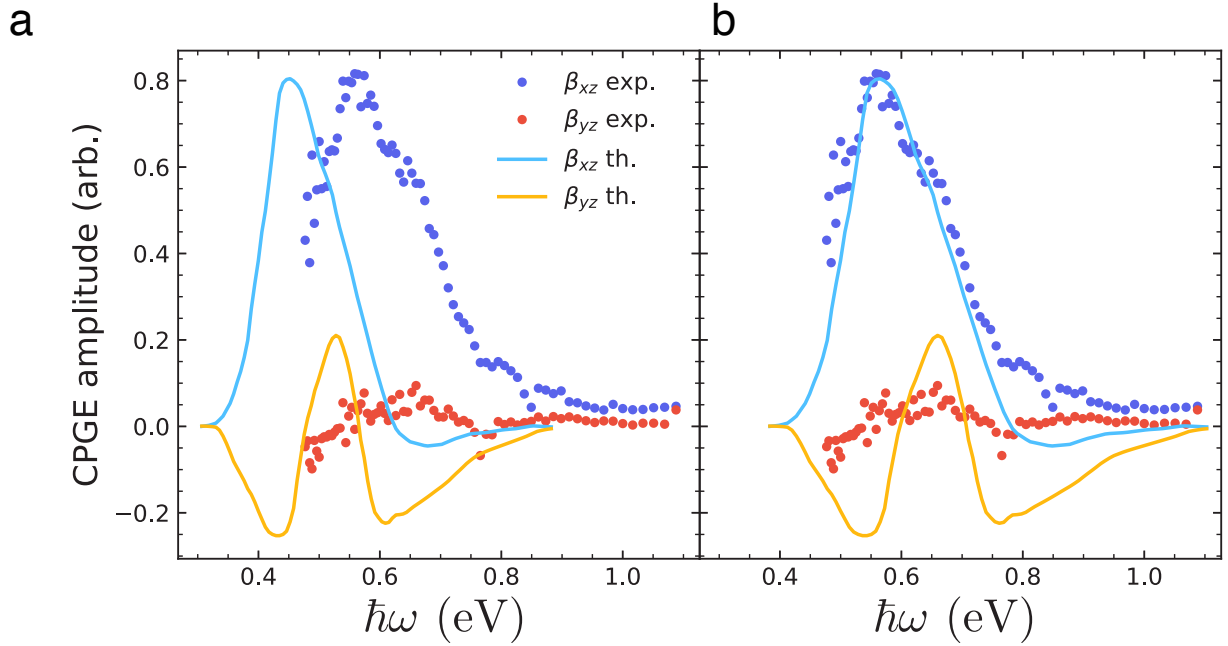


Figure 4.7: **CPGE spectrum on (001)** (a) CPGE spectral data for β_{xz} and β_{yz} compared with theory from Ref. [13]. (b) Experimental data compared with theory after rescaling of energy. Rescaling of the energy by a factor 1.25 is seen when DFT/LDA theory is augmented by inclusion of a certain amount of Hartree-Fock exchange using hybrid density functionals, for example in the Heyd, Scuseria, and Ernzerhof (HSE) approach.

For each terahertz polarization (H or V), the set of data has three free parameters, illustrated simply by a sine wave plus an offset with parameters A , ϕ and C : $A \sin(2\theta + \phi) + C$. Thus, for two terahertz polarizations, we have six free variables and can thus determine the tensor parameters γ_{ijk} for $ijk = xxx, xxy, xyy, yxx, yxy, yyy$. Note that $\gamma_{ixy} = \gamma_{iyx}$. Data for multiple wavelengths is shown in Fig. 4.9.

We can determine the same set of six parameters by keeping the pump polarization fixed at $\theta = 0$ and instead rotating the sample axis about the surface normal by angle η . The two terahertz components measured will be

$$J_x(\eta) = \left[\gamma_{xxx} \cos^3 \eta - (\gamma_{xxy} + \gamma_{xyx} + \gamma_{yxx}) \cos^2 \eta \sin \eta + (\gamma_{xyy} + \gamma_{yxy} + \gamma_{yyx}) \cos \eta \sin^2 \eta - \gamma_{yyy} \sin^3 \eta \right] E_0^2 \quad (4.3)$$

and

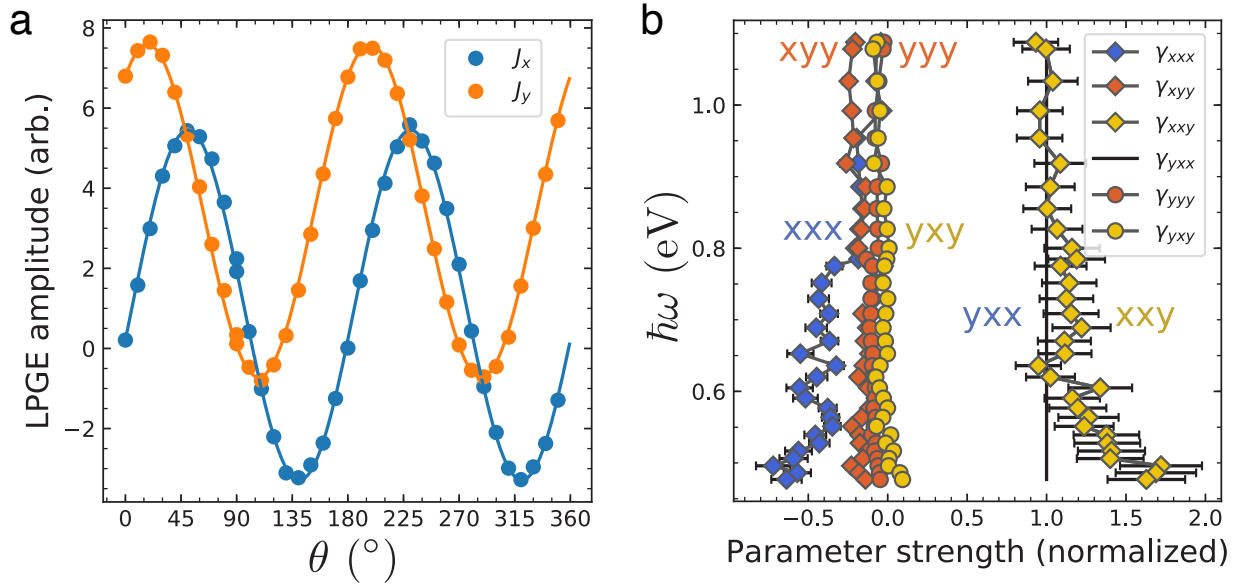


Figure 4.8: **LPGE on (001)** (a) Terahertz amplitude along x and y as a function of linear pump polarization angle θ for $\lambda = 2000\text{nm}$. (b) Results of fitting data in (a) to general LPGE tensor γ_{ijk} .

$$J_y(\eta) = \left[\gamma_{yxx} \cos^3 \eta + (\gamma_{xx} - \gamma_{yxy} - \gamma_{yyx}) \cos^2 \eta \sin \eta + (\gamma_{yyy} - \gamma_{xxy} - \gamma_{xyx}) \cos \eta \sin^2 \eta - \gamma_{xyy} \sin^3 \eta \right] E_0^2. \quad (4.4)$$

This allows us to use two different measurement methods to determine the same set of parameters γ_{ijk} .

Fig. 4.8(b) shows the relative amplitude of the six elements of γ_{ijk} (normalized to γ_{yxx}) in the photon energy range from 0.5 to 1.1 eV, along with error bars deriving from systematic errors. A striking feature of the spectra is that the response at photon energies above ~ 0.6 eV is dominated by two approximately equal components, $\gamma_{yxx} \approx \gamma_{xxy}$, with the other four close to zero, despite the fact that all six tensor components are in principle symmetry allowed. We note that the vanishing of components with an odd number of x indices would suggest a mirror symmetry $x \rightarrow -x$. A CPGE current directed along the x axis would be consistent with this symmetry. While the components appear to approximately obey such a symmetry, we know of no mechanism which would enforce this. We performed AFM measurements over two $5 \times 5 \mu\text{m}^2$ regions and two $1 \times 1 \mu\text{m}^2$ regions that reveal no patterns

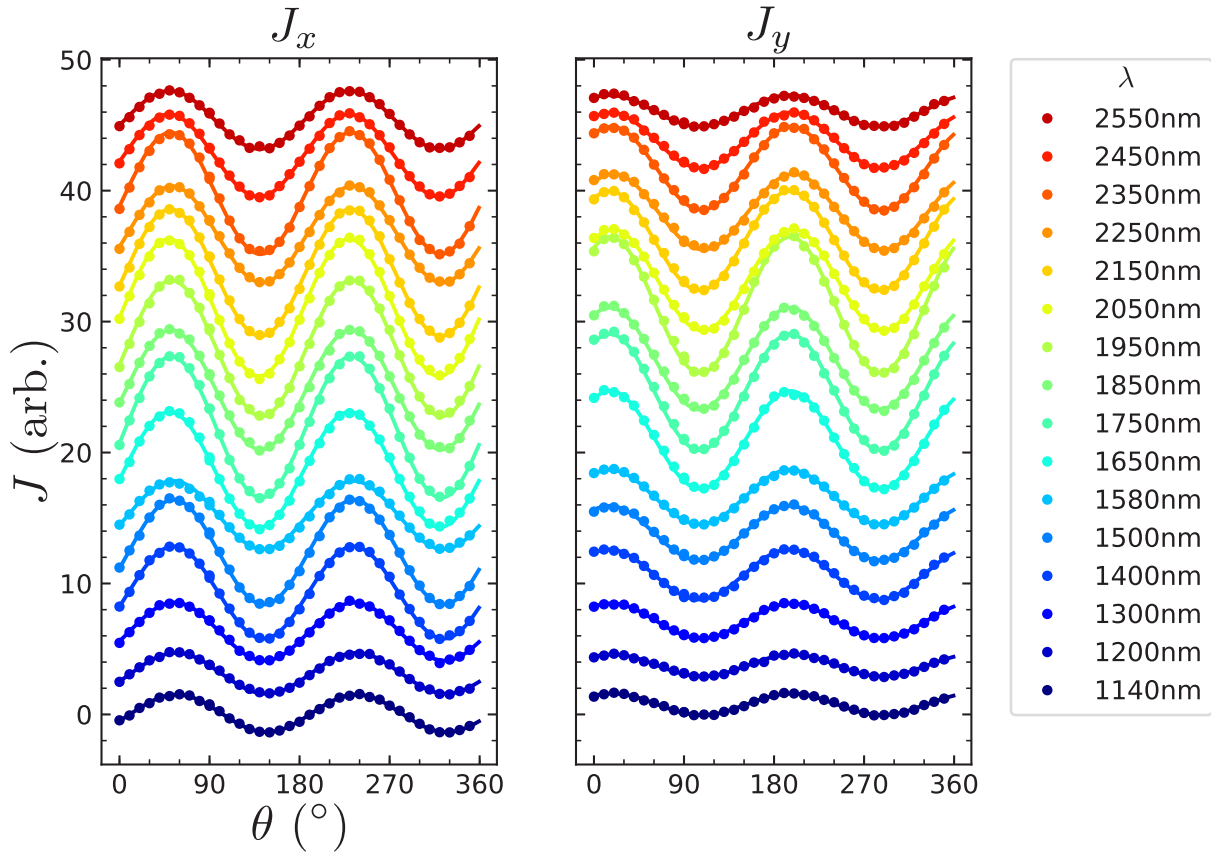


Figure 4.9: **Full LPGE scans on (001) LPGE measurements on RhSi 001 surface as a function of pump polarization angle for x and y components of terahertz.**

in surface topography that could affect the amplitude of photocurrents (Fig. 4.10). A surface variation of approximately 5 nm is observed.

In-plane mirror symmetry

Consider a general nonlinear tensor σ that describes the optical response in a material such that $J_i = \sigma_{ijk} E_j E_k$. We will consider the constraints on σ imposed by a symmetry of the mirror operation

$$M^x = \begin{pmatrix} -1 & 0 \\ 0 & 1 \end{pmatrix} \quad (4.5)$$

where we are restricting ourselves to 2D.

Under an operator \mathcal{O} , σ will transform as

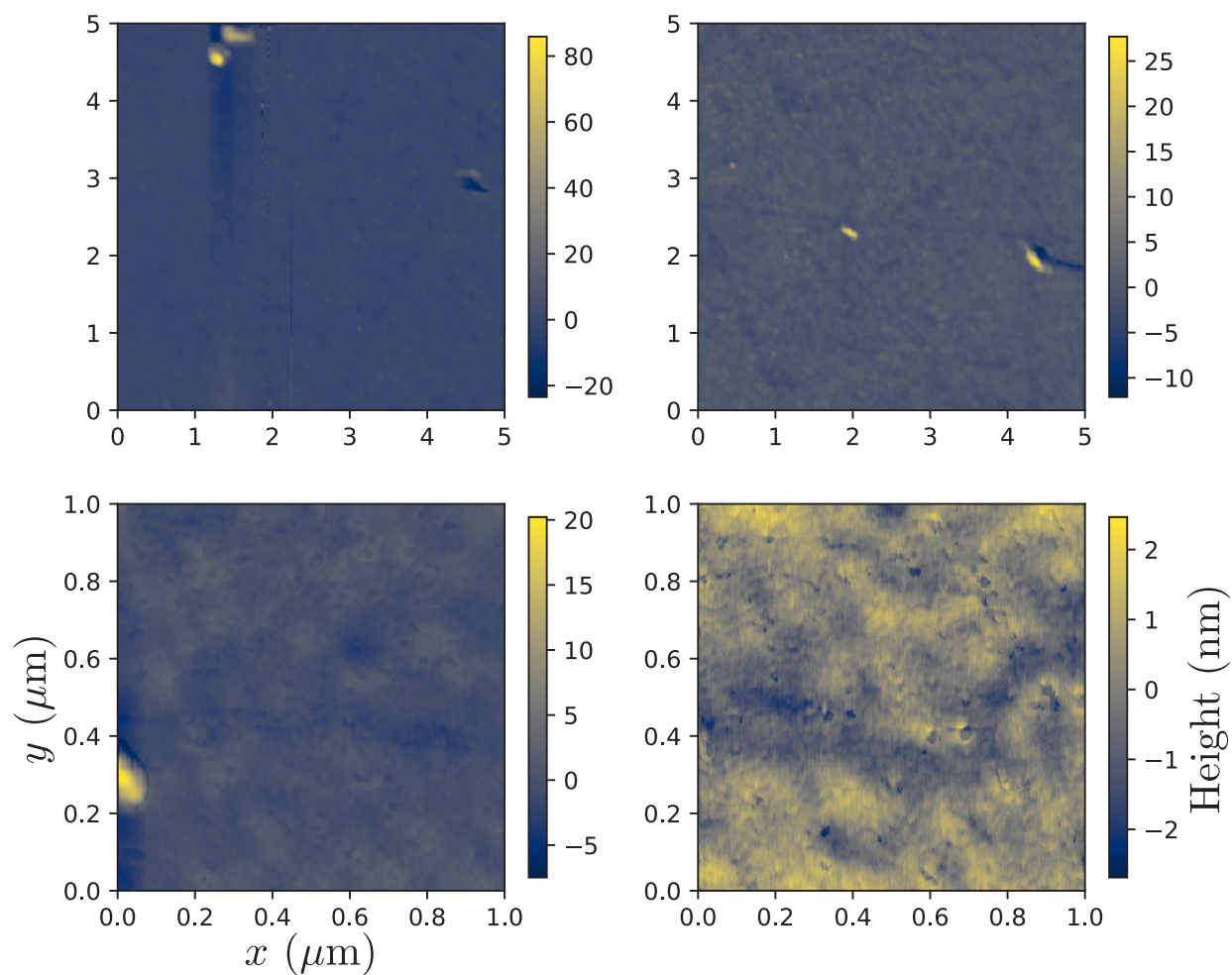


Figure 4.10: **AFM** Four AFM measurements on RhSi (001) surface showing crystal topography.

$$\sigma'_{ijk} = \mathcal{O}_{i\alpha} \mathcal{O}_{j\beta} \mathcal{O}_{k\gamma} \sigma_{\alpha\beta\gamma}. \quad (4.6)$$

When \mathcal{O} is a symmetry of the material in question, the constraint $\sigma'_{ijk} = \sigma_{ijk}$ is imposed. For $\mathcal{O} = M^x$, we arrive at the set of equations

$$\begin{aligned} \sigma'_{xxx} &= (M_{xx}^x)^3 \sigma_{xxx} = -\sigma_{xxx} = \sigma_{xxx} & (*) \\ \sigma'_{xxy} &= (M_{xx}^x)^2 M_{yy}^x \sigma_{xxy} = \sigma_{xxy} = \sigma_{xxy} \\ \sigma'_{xyy} &= M_{xx}^x (M_{yy}^x)^2 \sigma_{xyy} = -\sigma_{xyy} = \sigma_{xyy} & (*) \\ \sigma'_{yxx} &= (M_{xx}^x)^2 M_{yy}^x \sigma_{yxx} = \sigma_{yxx} = \sigma_{yxx} \\ \sigma'_{yyx} &= M_{xx}^x (M_{yy}^x)^2 \sigma_{yyx} = -\sigma_{yyx} = \sigma_{yyx} & (*) \\ \sigma'_{yyy} &= (M_{yy}^x)^3 \sigma_{yyy} = \sigma_{yyy} = \sigma_{yyy} \end{aligned} \quad (4.7)$$

The starred equations indicate elements that we find are equal to their own negative and therefore must be zero. We can conclude that for mirror symmetry M^x , the elements σ_{xxx} , σ_{xyy} and σ_{yyx} must be zero.

In conclusion, our measurements provide strong evidence in support of the prediction [13] of a new path to selective probing of the topological surface states in Weyl semimetals. We have observed LPGE and CPGE that arise selectively from surface states in chiral RhSi by choosing a configuration in which the response of the bulk is forbidden by symmetry. The CPGE spectrum, after a 25% rescaling of the energy axis, showed striking agreement with the response predicted for transitions between the spin polarized helicoidal bands that give rise to Fermi arcs [13]. LPGE measurements also probed the nonlinear response of surface states. An unanticipated result was that over a broad photon energy range only two elements of the nonlinear response tensor, γ_{ijk} , were required to fit the data, despite the six potentially nonzero elements expected by the C_1 surface symmetry. This result presents a challenge to theory of surface states in Weyl semimetals. Finally, the measurement scheme demonstrated here offers a general approach to selectively probe surface states of topological matter through the use of nonlinear optical effects in which the response of the bulk vanishes by symmetry.

Bibliography

- [1] N. P. Armitage, E. J. Mele, and Ashvin Vishwanath. “Weyl and Dirac semimetals in three-dimensional solids”. In: *Rev. Mod. Phys.* 90 (1 Jan. 2018), p. 015001. DOI: 10.1103/RevModPhys.90.015001. URL: <https://link.aps.org/doi/10.1103/RevModPhys.90.015001>.
- [2] V. M. Asnin et al. ““Circular” Photogalvanic Effect in Optically Active Crystals”. In: *The Physics of Selenium and Tellurium*. Ed. by E. Gerlach and P. Grosse. Berlin, Heidelberg: Springer Berlin Heidelberg, 1979, pp. 116–118. ISBN: 978-3-642-81398-6.
- [3] H. J. Bakker et al. “Distortion of terahertz pulses in electro-optic sampling”. In: *J. Opt. Soc. Am. B* 15.6 (June 1998), pp. 1795–1801. DOI: 10.1364/JOSAB.15.001795. URL: <http://josab.osa.org/abstract.cfm?URI=josab-15-6-1795>.
- [4] V. I. Belinicher and B. I. Sturman. “The photogalvanic effect in media lacking a center of symmetry”. In: *Phys. Usp.* 23.3 (1980), pp. 199–223. URL: <https://ufn.ru/en/articles/1980/3/b/>.
- [5] Ilya Belopolski et al. “Criteria for Directly Detecting Topological Fermi Arcs in Weyl Semimetals”. In: *Phys. Rev. Lett.* 116 (6 Feb. 2016), p. 066802. DOI: 10.1103/PhysRevLett.116.066802. URL: <https://link.aps.org/doi/10.1103/PhysRevLett.116.066802>.
- [6] Michael Victor Berry. “Quantal phase factors accompanying adiabatic changes”. In: *Proceedings of the Royal Society of London. A. Mathematical and Physical Sciences* 392.1802 (1984), pp. 45–57. DOI: 10.1098/rspa.1984.0023.
- [7] Robert W. Boyd. *Nonlinear Optics*. Third Edition. Academic Press, 2008.
- [8] Barry Bradlyn et al. “Beyond Dirac and Weyl fermions: Unconventional quasiparticles in conventional crystals”. In: *Science* 353.6299 (2016). ISSN: 0036-8075. DOI: 10.1126/science.aaf5037. URL: <http://science.sciencemag.org/content/353/6299/aaf5037>.
- [9] Fabian D. J. Brunner et al. “Distortion-free enhancement of terahertz signals measured by electro-optic sampling. I. Theory”. In: *J. Opt. Soc. Am. B* 31.4 (Apr. 2014), pp. 904–910. DOI: 10.1364/JOSAB.31.000904. URL: <http://josab.osa.org/abstract.cfm?URI=josab-31-4-904>.

- [10] Ching-Kit Chan et al. “Photocurrents in Weyl semimetals”. In: *Phys. Rev. B* 95 (4 Jan. 2017), p. 041104. DOI: 10.1103/PhysRevB.95.041104. URL: <https://link.aps.org/doi/10.1103/PhysRevB.95.041104>.
- [11] Guoqing Chang et al. “Topological quantum properties of chiral crystals”. In: *Nature Materials* 17.11 (2018), pp. 978–985. ISSN: 1476-4660. DOI: 10.1038/s41563-018-0169-3. URL: <https://doi.org/10.1038/s41563-018-0169-3>.
- [12] Guoqing Chang et al. “Unconventional Chiral Fermions and Large Topological Fermi Arcs in RhSi”. In: *Phys. Rev. Lett.* 119 (20 Nov. 2017), p. 206401. DOI: 10.1103/PhysRevLett.119.206401. URL: <https://link.aps.org/doi/10.1103/PhysRevLett.119.206401>.
- [13] Guoqing Chang et al. “Unconventional Photocurrents from Surface Fermi Arcs in Topological Chiral Semimetals”. In: *Phys. Rev. Lett.* 124 (16 Apr. 2020), p. 166404. DOI: 10.1103/PhysRevLett.124.166404. URL: <https://link.aps.org/doi/10.1103/PhysRevLett.124.166404>.
- [14] Tyler A. Cochran et al. “A Fermi Arc Quantum Ladder”. In: *arXiv* (2020). arXiv: 2004.11365 [cond-mat.mtrl-sci].
- [15] Chen Fang et al. “Topological semimetals with helicoid surface states”. In: *Nature Physics* 12.10 (2016), pp. 936–941. ISSN: 1745-2481. DOI: 10.1038/nphys3782. URL: <https://doi.org/10.1038/nphys3782>.
- [16] HD Flack. “On enantiomorph-polarity estimation”. In: *Acta Crystallographica Section A: Foundations of Crystallography* 39.6 (1983), pp. 876–881.
- [17] Felix Flicker et al. “Chiral optical response of multifold fermions”. In: *Phys. Rev. B* 98 (15 Oct. 2018), p. 155145. DOI: 10.1103/PhysRevB.98.155145. URL: <https://link.aps.org/doi/10.1103/PhysRevB.98.155145>.
- [18] Liang Fu, C. L. Kane, and E. J. Mele. “Topological Insulators in Three Dimensions”. In: *Phys. Rev. Lett.* 98 (10 Mar. 2007), p. 106803. DOI: 10.1103/PhysRevLett.98.106803. URL: <https://link.aps.org/doi/10.1103/PhysRevLett.98.106803>.
- [19] G. Gallot and D. Grischkowsky. “Electro-optic detection of terahertz radiation”. In: *J. Opt. Soc. Am. B* 16.8 (Aug. 1999), pp. 1204–1212. DOI: 10.1364/JOSAB.16.001204. URL: <http://josab.osa.org/abstract.cfm?URI=josab-16-8-1204>.
- [20] S D Ganichev and W Prettl. “Spin photocurrents in quantum wells”. In: *Journal of Physics: Condensed Matter* 15.20 (May 2003), R935–R983. DOI: 10.1088/0953-8984/15/20/204. URL: <https://doi.org/10.1088/0953-8984/15/20/204>.
- [21] S. D. Ganichev et al. “Resonant inversion of the circular photogalvanic effect in n-doped quantum wells”. In: *Phys. Rev. B* 68 (3 July 2003), p. 035319. DOI: 10.1103/PhysRevB.68.035319. URL: <https://link.aps.org/doi/10.1103/PhysRevB.68.035319>.

- [22] Y Gao et al. “Chiral terahertz wave emission from the Weyl semimetal TaAs”. In: *Nature Communications* 11.1 (2020), p. 720. ISSN: 2041-1723. DOI: 10.1038/s41467-020-14463-1. URL: <https://doi.org/10.1038/s41467-020-14463-1>.
- [23] Sayandip Ghosh and Carsten Timm. “Dynamical density and spin response of Fermi arcs and their consequences for Weyl semimetals”. In: *Phys. Rev. B* 101 (16 Apr. 2020), p. 165402. DOI: 10.1103/PhysRevB.101.165402. URL: <https://link.aps.org/doi/10.1103/PhysRevB.101.165402>.
- [24] M. Z. Hasan and C. L. Kane. “Colloquium: Topological insulators”. In: *Rev. Mod. Phys.* 82 (4 Nov. 2010), pp. 3045–3067. DOI: 10.1103/RevModPhys.82.3045. URL: <https://link.aps.org/doi/10.1103/RevModPhys.82.3045>.
- [25] M. Zahid Hasan et al. “Discovery of Weyl Fermion Semimetals and Topological Fermi Arc States”. In: *Annual Review of Condensed Matter Physics* 8.1 (2017), pp. 289–309. DOI: 10.1146/annurev-conmatphys-031016-025225. eprint: <https://doi.org/10.1146/annurev-conmatphys-031016-025225>. URL: <https://doi.org/10.1146/annurev-conmatphys-031016-025225>.
- [26] Pavan Hosur. “Circular photogalvanic effect on topological insulator surfaces: Berry-curvature-dependent response”. In: *Phys. Rev. B* 83 (3 Jan. 2011), p. 035309. DOI: 10.1103/PhysRevB.83.035309. URL: <https://link.aps.org/doi/10.1103/PhysRevB.83.035309>.
- [27] D Hsieh et al. “A topological Dirac insulator in a quantum spin Hall phase”. In: *Nature* 452.7190 (2008), pp. 970–974. ISSN: 1476-4687. DOI: 10.1038/nature06843. URL: <https://doi.org/10.1038/nature06843>.
- [28] Hiroyuki Inoue et al. “Quasiparticle interference of the Fermi arcs and surface-bulk connectivity of a Weyl semimetal”. In: *Science* 351.6278 (2016), pp. 1184–1187. ISSN: 0036-8075. DOI: 10.1126/science.aad8766. eprint: <https://science.sciencemag.org/content/351/6278/1184.full.pdf>. URL: <https://science.sciencemag.org/content/351/6278/1184>.
- [29] E. L. Ivchenko and S. D. Ganichev. *Spin-dependent photogalvanic effects (A Review)*. 2017. arXiv: 1710.09223 [cond-mat.mes-hall].
- [30] E. L. Ivchenko and G. E. Pikus. “Photogalvanic effects in optically active crystals”. In: *Ferroelectrics* 43.1 (1982), pp. 131–136. DOI: 10.1080/00150198208210632. eprint: <https://doi.org/10.1080/00150198208210632>. URL: <https://doi.org/10.1080/00150198208210632>.
- [31] Zhurun Ji et al. “Spatially dispersive circular photogalvanic effect in a Weyl semimetal”. In: *Nature Materials* (2019). ISSN: 1476-4660. DOI: 10.1038/s41563-019-0421-5. URL: <https://doi.org/10.1038/s41563-019-0421-5>.
- [32] Shuang Jia, Su-Yang Xu, and M Zahid Hasan. “Weyl semimetals, Fermi arcs and chiral anomalies”. In: *Nature Materials* 15.11 (2016), pp. 1140–1144. ISSN: 1476-4660. DOI: 10.1038/nmat4787. URL: <https://doi.org/10.1038/nmat4787>.

- [33] Jeremy A. Johnson et al. “Distortion-free enhancement of terahertz signals measured by electro-optic sampling. II. Experiment”. In: *J. Opt. Soc. Am. B* 31.5 (May 2014), pp. 1035–1040. DOI: 10.1364/JOSAB.31.001035. URL: <http://josab.osa.org/abstract.cfm?URI=josab-31-5-1035>.
- [34] F. de Juan et al. “Difference frequency generation in topological semimetals”. In: *Phys. Rev. Research* 2 (1 Jan. 2020), p. 012017. DOI: 10.1103/PhysRevResearch.2.012017. URL: <https://link.aps.org/doi/10.1103/PhysRevResearch.2.012017>.
- [35] Fernando de Juan et al. “Quantized circular photogalvanic effect in Weyl semimetals”. In: *Nature Communications* 8 (July 2017), p. 15995. URL: <https://doi.org/10.1038/ncomms15995><http://10.0.4.14/ncomms15995><https://www.nature.com/articles/ncomms15995>[7B%5C%7Dsupplementary-information](https://www.nature.com/articles/ncomms15995#supplementary-information).
- [36] Tosio Kato. “On the Adiabatic Theorem of Quantum Mechanics”. In: *Journal of the Physical Society of Japan* 5.6 (1950), pp. 435–439. DOI: 10.1143/JPSJ.5.435. URL: <https://doi.org/10.1143/JPSJ.5.435>.
- [37] Congcong Le et al. “Ab initio study of quantized circular photogalvanic effect in chiral multifold semimetals”. In: *Phys. Rev. B* 102 (12 Sept. 2020), p. 121111. DOI: 10.1103/PhysRevB.102.121111. URL: <https://link.aps.org/doi/10.1103/PhysRevB.102.121111>.
- [38] Hang Li et al. “Chiral fermion reversal in chiral crystals”. In: *Nature Communications* 10.1 (2019), p. 5505. ISSN: 2041-1723. DOI: 10.1038/s41467-019-13435-4. URL: <https://doi.org/10.1038/s41467-019-13435-4>.
- [39] Jing Liu et al. “Semimetals for high-performance photodetection”. In: *Nature Materials* 19.8 (2020), pp. 830–837. ISSN: 1476-4660. DOI: 10.1038/s41563-020-0715-7. URL: <https://doi.org/10.1038/s41563-020-0715-7>.
- [40] B. Q. Lv et al. “Experimental Discovery of Weyl Semimetal TaAs”. In: *Phys. Rev. X* 5 (3 July 2015), p. 031013. DOI: 10.1103/PhysRevX.5.031013. URL: <https://link.aps.org/doi/10.1103/PhysRevX.5.031013>.
- [41] Junchao Ma et al. “Nonlinear photoresponse of type-II Weyl semimetals”. In: *Nature Materials* 18.5 (2019), pp. 476–481. ISSN: 14764660. DOI: 10.1038/s41563-019-0296-5. URL: <https://doi.org/10.1038/s41563-019-0296-5>.
- [42] Qiong Ma, Adolfo G Grushin, and Kenneth S Burch. “Topology and geometry under the nonlinear electromagnetic spotlight”. In: *Nature Materials* (2021). ISSN: 1476-4660. DOI: 10.1038/s41563-021-00992-7. URL: <https://doi.org/10.1038/s41563-021-00992-7>.
- [43] Qiong Ma et al. “Direct optical detection of Weyl fermion chirality in a topological semimetal”. In: *Nature Physics* 13 (May 2017), p. 842. URL: <https://doi.org/10.1038/nphys4146><http://10.0.4.14/nphys4146><https://www.nature.com/articles/nphys4146>[7B%5C%7Dsupplementary-information](https://www.nature.com/articles/nphys4146#supplementary-information).

- [44] L. Z. Maulana et al. “Optical conductivity of multifold fermions: The case of RhSi”. In: *Phys. Rev. Research* 2 (2 Apr. 2020), p. 023018. DOI: 10.1103/PhysRevResearch.2.023018. URL: <https://link.aps.org/doi/10.1103/PhysRevResearch.2.023018>.
- [45] Philip J W Moll et al. “Transport evidence for Fermi-arc-mediated chirality transfer in the Dirac semimetal Cd₃As₂”. In: *Nature* 535.7611 (2016), pp. 266–270. ISSN: 1476-4687. DOI: 10.1038/nature18276. URL: <https://doi.org/10.1038/nature18276>.
- [46] Dibya Kanti Mukherjee, David Carpentier, and Mark Oliver Goerbig. “Dynamical conductivity of the Fermi arc and the Volkov-Pankratov states on the surface of Weyl semimetals”. In: *Phys. Rev. B* 100 (19 Nov. 2019), p. 195412. DOI: 10.1103/PhysRevB.100.195412. URL: <https://link.aps.org/doi/10.1103/PhysRevB.100.195412>.
- [47] Ajay Nahata, Aniruddha S. Weling, and Tony F. Heinz. “A wideband coherent terahertz spectroscopy system using optical rectification and electro-optic sampling”. In: *Applied Physics Letters* 69.16 (1996), pp. 2321–2323. DOI: 10.1063/1.117511. eprint: <https://doi.org/10.1063/1.117511>. URL: <https://doi.org/10.1063/1.117511>.
- [48] Zhuoliang Ni et al. “Linear and nonlinear optical responses in the chiral multifold semimetal RhSi”. In: *npj Quantum Materials* 5.1 (2020), p. 96. ISSN: 2397-4648. DOI: 10.1038/s41535-020-00298-y. URL: <https://doi.org/10.1038/s41535-020-00298-y>.
- [49] H.B. Nielsen and Masao Ninomiya. “The Adler-Bell-Jackiw anomaly and Weyl fermions in a crystal”. In: *Physics Letters B* 130.6 (1983), pp. 389–396. ISSN: 0370-2693. DOI: [https://doi.org/10.1016/0370-2693\(83\)91529-0](https://doi.org/10.1016/0370-2693(83)91529-0). URL: <http://www.sciencedirect.com/science/article/pii/0370269383915290>.
- [50] J. Orenstein et al. “Topology and Symmetry of Quantum Materials via Nonlinear Optical Responses”. In: *Annual Review of Condensed Matter Physics* 12.1 (2021), pp. 247–272. DOI: 10.1146/annurev-conmatphys-031218-013712. eprint: <https://doi.org/10.1146/annurev-conmatphys-031218-013712>. URL: <https://doi.org/10.1146/annurev-conmatphys-031218-013712>.
- [51] Gavin B. Osterhoudt et al. “Colossal mid-infrared bulk photovoltaic effect in a type-I Weyl semimetal”. In: *Nature Materials* 18.5 (2019), pp. 471–475. ISSN: 14764660. DOI: 10.1038/s41563-019-0297-4. URL: <https://doi.org/10.1038/s41563-019-0297-4>.
- [52] H. Plank et al. “Infrared/terahertz spectra of the photogalvanic effect in (Bi,Sb)Te based three-dimensional topological insulators”. In: *Phys. Rev. Materials* 2 (2 Feb. 2018), p. 024202. DOI: 10.1103/PhysRevMaterials.2.024202. URL: <https://link.aps.org/doi/10.1103/PhysRevMaterials.2.024202>.
- [53] Andrew C Potter, Itamar Kimchi, and Ashvin Vishwanath. “Quantum oscillations from surface Fermi arcs in Weyl and Dirac semimetals”. In: *Nature communications* 5.1 (2014), pp. 1–6.

- [54] Xiao-Liang Qi and Shou-Cheng Zhang. “Topological insulators and superconductors”. In: *Rev. Mod. Phys.* 83 (4 Oct. 2011), pp. 1057–1110. DOI: 10.1103/RevModPhys.83.1057. URL: <https://link.aps.org/doi/10.1103/RevModPhys.83.1057>.
- [55] Dylan Rees et al. “Helicity-dependent photocurrents in the chiral Weyl semimetal RhSi”. In: *Science Advances* 6.29 (2020). DOI: 10.1126/sciadv.aba0509. eprint: <https://advances.sciencemag.org/content/6/29/eaba0509.full.pdf>. URL: <https://advances.sciencemag.org/content/6/29/eaba0509>.
- [56] Miguel-Ángel Sánchez-Martínez, Fernando de Juan, and Adolfo G. Grushin. “Linear optical conductivity of chiral multifold fermions”. In: *Phys. Rev. B* 99 (15 Apr. 2019), p. 155145. DOI: 10.1103/PhysRevB.99.155145. URL: <https://link.aps.org/doi/10.1103/PhysRevB.99.155145>.
- [57] Daniel S. Sanchez et al. “Topological chiral crystals with helicoid-arc quantum states”. In: *Nature* 567.7749 (2019), pp. 500–505. ISSN: 14764687. DOI: 10.1038/s41586-019-1037-2. URL: <https://doi.org/10.1038/s41586-019-1037-2>.
- [58] Niels B.M. Schröter et al. “Chiral topological semimetal with multifold band crossings and long Fermi arcs”. In: *Nature Physics* (2019). ISSN: 17452481. DOI: 10.1038/s41567-019-0511-y. URL: <https://doi.org/10.1038/s41567-019-0511-y>.
- [59] Li-kun Shi and Justin C. W. Song. “Large optical conductivity of Dirac semimetal Fermi arc surface states”. In: *Phys. Rev. B* 96 (8 Aug. 2017), p. 081410. DOI: 10.1103/PhysRevB.96.081410. URL: <https://link.aps.org/doi/10.1103/PhysRevB.96.081410>.
- [60] N. Sirica et al. “Tracking Ultrafast Photocurrents in the Weyl Semimetal TaAs Using THz Emission Spectroscopy”. In: *Phys. Rev. Lett.* 122 (19 May 2019), p. 197401. DOI: 10.1103/PhysRevLett.122.197401. URL: <https://link.aps.org/doi/10.1103/PhysRevLett.122.197401>.
- [61] Justin C. W. Song and Mark S. Rudner. “Fermi arc plasmons in Weyl semimetals”. In: *Phys. Rev. B* 96 (20 Nov. 2017), p. 205443. DOI: 10.1103/PhysRevB.96.205443. URL: <https://link.aps.org/doi/10.1103/PhysRevB.96.205443>.
- [62] Kai Sun et al. “Circular Photogalvanic Effect in the Weyl Semimetal TaAs”. In: *Chinese Physics Letters* 34.11 (Nov. 2017), p. 117203. DOI: 10.1088/0256-307x/34/11/117203. URL: <https://doi.org/10.1088/0256-307x/34/11/117203>.
- [63] Daichi Takane et al. “Observation of Chiral Fermions with a Large Topological Charge and Associated Fermi-Arc Surface States in CoSi”. In: *Phys. Rev. Lett.* 122 (7 Feb. 2019), p. 076402. DOI: 10.1103/PhysRevLett.122.076402. URL: <https://link.aps.org/doi/10.1103/PhysRevLett.122.076402>.
- [64] Peizhe Tang, Quan Zhou, and Shou-Cheng Zhang. “Multiple Types of Topological Fermions in Transition Metal Silicides”. In: *Phys. Rev. Lett.* 119 (20 Nov. 2017), p. 206402. DOI: 10.1103/PhysRevLett.119.206402. URL: <https://link.aps.org/doi/10.1103/PhysRevLett.119.206402>.

- [65] Xiangang Wan et al. “Topological semimetal and Fermi-arc surface states in the electronic structure of pyrochlore iridates”. In: *Phys. Rev. B* 83 (20 May 2011), p. 205101. DOI: 10.1103/PhysRevB.83.205101. URL: <https://link.aps.org/doi/10.1103/PhysRevB.83.205101>.
- [66] Dennis Wawrzik et al. “Infinite Berry Curvature of Weyl Fermi Arcs”. In: *Phys. Rev. Lett.* 127 (5 July 2021), p. 056601. DOI: 10.1103/PhysRevLett.127.056601. URL: <https://link.aps.org/doi/10.1103/PhysRevLett.127.056601>.
- [67] Di Xiao, Ming-Che Chang, and Qian Niu. “Berry phase effects on electronic properties”. In: *Rev. Mod. Phys.* 82 (3 July 2010), pp. 1959–2007. DOI: 10.1103/RevModPhys.82.1959. URL: <https://link.aps.org/doi/10.1103/RevModPhys.82.1959>.
- [68] Su-Yang Xu et al. “Discovery of a Weyl fermion semimetal and topological Fermi arcs”. In: *Science* 349.6248 (2015), pp. 613–617. ISSN: 0036-8075. DOI: 10.1126/science.aaa9297. eprint: <https://science.sciencemag.org/content/349/6248/613.full.pdf>. URL: <https://science.sciencemag.org/content/349/6248/613>.
- [69] Su-Yang Xu et al. “Observation of Fermi arc surface states in a topological metal”. In: *Science* 347.6219 (2015), pp. 294–298. ISSN: 0036-8075. DOI: 10.1126/science.1256742. eprint: <https://science.sciencemag.org/content/347/6219/294.full.pdf>. URL: <https://science.sciencemag.org/content/347/6219/294>.